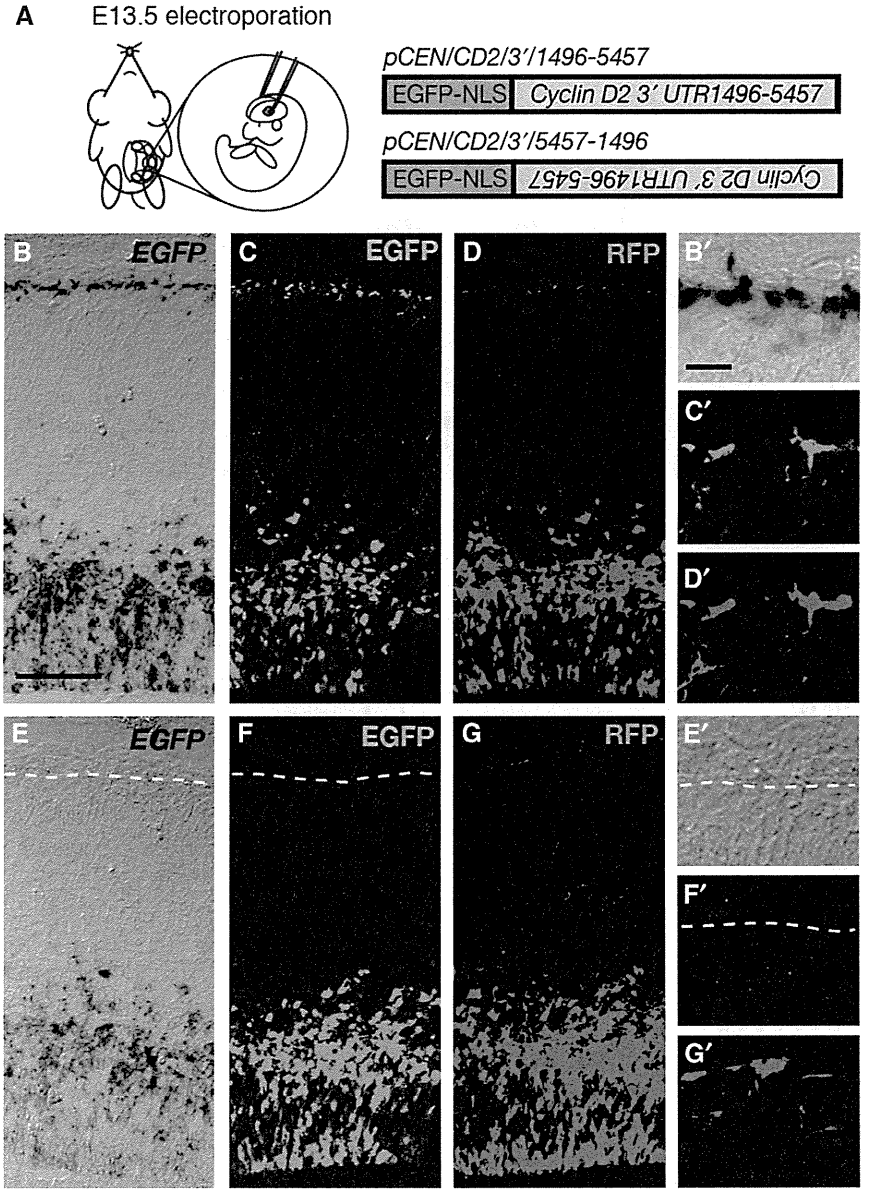

Figure 3 Reporter mRNAs carrying *Cyclin D2* 3′UTR transport element are directed to the basal endfeet and translated locally. (**A**) EGFP constructs carrying Cyclin D2 transport element in forward and reverse orientation (*pCEN/CD2/3′/1496-5457* and *pCEN/CD2/3′/5457-1496*) were introduced into the E13.5 mouse neocortex by *in-utero* electroporation, together with *pCAGGS-mRFP*. (**B**–**G**) Analysis 24 h later shows that mRNA for EGFP, from *pCEN/CD2/3′/1496-5457*, is expressed at the basal endfeet of radial glia (**B** and **B'**). Conversely, *EGFP* mRNA from *pCEN/CD2/3′/5457-1496* is absent from the basal endfeet (**E** and **E'**). At the protein level, EGFP translated from *pCEN/CD2/3′/1496-5457* is present at the basal endfoot and VZ cells (**C** and **C'**), whereas EGFP from the reversed *pCEN/CD2/3′/5457-1496* is present only in the VZ but undetected in the basal endfoot (**F** and **F'**). Co-transfection with RFP indicates that the reporter protein can be visibly observed in the basal processes and endfeet (**D**, **D'**, **G** and **G'**). Scale bars: 100 μm in (**B**–**G**) and 10 μm in (**B'**–**G'**).

hemisphere, or neighbouring clusters with sufficient separation to be considered as clonal (refer to Supplementary Figure S4). To clearly identify the progenitor cell with its attached basal process, we performed three-dimensional reconstruction of individual daughter cells using Z-stacked images ($n=28$) (a representative image is shown in Supplementary Movie 1). This analysis has revealed that most of the basal processes are inherited by basally positioned daughter cells (26/28) as previously reported (Ochiai *et al*, 2009).

A transfection protocol was employed to express EGFP in the basal process and immunostaining for Cyclin D2 was conducted to detect protein distribution at different stages of the cell cycle (Figure 4). Cells in M phase were identified using an antibody against phospho-Vimentin (pVim) that stains M-phase cytoplasm and the basal fibres (Figure 4A; Kamei *et al*, 1998). At the M phase ($n=15$), Cyclin D2 was weakly expressed in the nucleus but strongly expressed in the basal process and endfoot (Figure 4A–D, M, and N). Thus, Cyclin D2 is continuously present in the basal endfoot of APs during the M phase.

To analyse early G1 to late G1 phase, 22 embryos at E12.5 were transfected with the reporter GFP vector. This yielded 19 daughter pairs sharing a single apical process and one basal

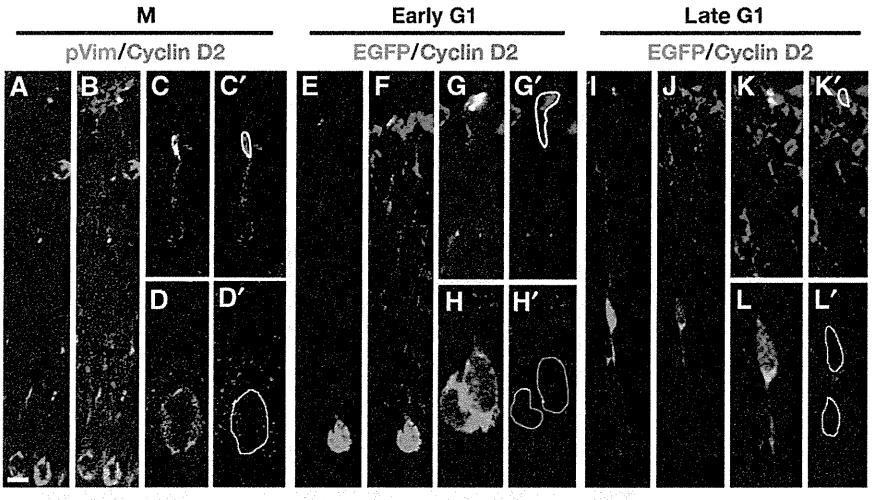

M

	Basal endfoot	Nucleus	
M	++	+	(*n*=15/15)
Eearly G1			
BD	++	+	(*n*=4/4)
AD	–	+	
Late G1			
BD	++	+	(*n*=10/15)
AD	–	–	
BD	++	+	(*n*=3/15)
AD	–	+	
BD	++	–	(*n*=1/15)
AD	–	+	
BD	+	–	(*n*=1/15)
AD	–	–	

BD = Basally positioned daughter cell
AD = Apically positioned daughter cell

N

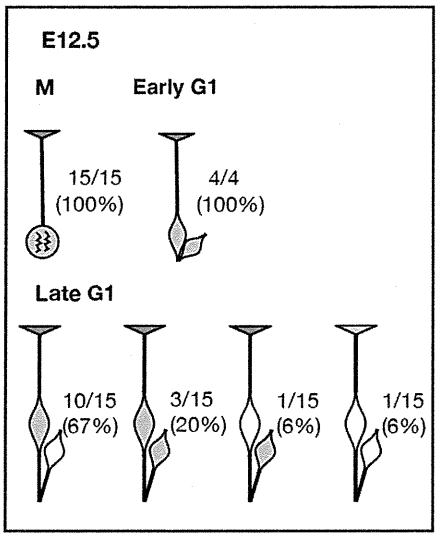

Figure 4 Location and inheritance of Cyclin D2 protein by clonal pairs during the cell cycle at E12.5 using an EGFP lentivirus. (**A–D'**) Identification of clones containing phospho-vimentin-positive M cells show weak Cyclin D2 distribution in the nucleus and basal endfoot. (**E–H'**) A single clone-derived pair of daughter cells anchored by an apical membrane were considered to be in early G1. (**G, H'**) are high-magnification images of centrally positioned cell body and a basal endfoot shown in (**C**). Cyclin D2 protein at this stage is present in the basal process attached to the basally positioned daughter whose nucleus is also stained for Cyclin D2. The apically positioned daughter is weakly positive for Cyclin D2. (**I–L'**) At late G1, Cyclin D2 is clearly expressed in the basal process and endfoot belonging to the basally positioned daughter (also stained for Cyclin D2). In contrast, the apically positioned daughter is devoid of Cyclin D2. (**M**) Summary of Cyclin D2 expression in the basal endfoot and nucleus in cells undergoing different stages of the cell cycle. (**N**) Schematic diagram of Cyclin D2 expression in the basal endfoot and nucleus at different cell-cycle stages. After asymmetric cell division, the majority (67%) of offspring in late G1 shows preferential staining of Cyclin D2 in the basal endfoot and nucleus belonging to the basally positioned daughter. Intensity of the staining is shown as + (modest) and + + (strong). Scale bar: 10 μm.

process inherited by one of the daughter cells and had therefore undergone asymmetric division (Figure 4E–N). To identify early G1 daughter pairs ($n=4$), we used the criterion of close proximity of the daughter cell body to the apical surface (Ochiai *et al*, 2009), and considered these daughter cells to have been born within a 0–3 h period if one of the two daughters was still anchored to the apical membrane (Figure 4E–H'). This analysis revealed that Cyclin D2 was only weakly expressed in both daughter cell bodies (Figure 4H, H', M, and N), but strongly expressed at the basal process and endfoot (Figure 4G, G', M, and N). By contrast, cells considered to be in late G1 (born greater than 3 h ago and no longer attached to the apical membrane) ($n=15$) showed four different patterns of Cyclin D2 inheritance (Figure 4I–N). In the majority pattern (67%; 10/15), stronger expression of Cyclin D2 was detected in the basally positioned daughter that also carried the basal process stained with Cyclin D2 in the endfoot (Figure 4M and N). Twenty percent of the pairs (3/15) showed equal expression of Cyclin D2 in both daughter cells, and one pair (6%) showed no expression Cyclin D2 in both daughter cells (Figure 4M and N). Finally, another pair (6%) displayed the opposite trend, with strong Cyclin D2 expression in the basal endfoot but no staining in its associated cell body, while the sister cell body without the basal process possessed Cyclin D2 (Figure 4M and N). Thus, Cyclin D2 presents in the basal process and endfoot during cell division, and after asymmetric

cell division, Cyclin D2 is more frequently segregated to the nucleus of the basally positioned daughter cell.

To further examine Cyclin D2 protein inheritance at later stages of neurogenesis (E14.5), E12.5 forebrains were infected with low titre EGFP lentivirus and sacrificed 48 h later (Supplementary Figure S4). Analysis of daughter pairs at early G1 (and therefore closer to the ventricle) showed a variable yet robust result, with 44% of the pairs (4/9) accumulating Cyclin D2 in the basally positioned daughter cell, while the remainder (5/9) showed no detectable Cyclin D2 expression in both daughter cells (Figure 5A–C'' and M). Daughter pairs considered to have undergone division >3 h prior to collection and situated at some distance from the apical membrane were considered to be in late G1. This analysis indicated that 100% of the late G1 daughter pairs (20/20) accumulated more Cyclin D2 protein in the basally positioned daughters (Figure 5D–F'' and M). In summary, these experiments are instructive regarding Cyclin D2 inheritance to daughter cells following apical progenitor divisions during early and mid neurogenesis. Interestingly, compared with earlier stages (E12.5; Figure 4N) a larger proportion of cells at late G1 inherited Cyclin D2 only in the basally positioned daughter (E14.5; Figure 5M). Taken together, this retrospective staining for Cyclin D2 suggests that preferential distribution of Cyclin D2 protein to one daughter cell is strongly associated with the acquisition of dissimilar daughter cell fates.

Previous studies suggest that apically positioned daughter cells acquire postmitotic neuronal characteristics, while basally positioned daughters tend to be self-renewing (Noctor *et al*, 2001; Konno *et al*, 2008; Ochiai *et al*, 2009). To test this, Ngn2, a marker for neuronal differentiation was used to examine Cyclin D2 inheritance patterns. At E12.5, all the daughter pairs (8/8) at early G1 were devoid of Ngn2 (Supplementary Figure S5A—C and G), a trend also observed at E14.5 (Figure 5G–I'' and N). In contrast to Cyclin D2, 50% of late G1 daughter pairs (9/18) showed Ngn2 accumulation in the apically positioned daughter cell at E12.5 (Supplementary Figure S5D–F and G), and 75% of pairs (12/6) at E14 (Figure 5J–L'' and N). Together, these results strongly point to the conclusion that by late G1, a consequence of asymmetric division is the differential allocation of Cyclin D2 to the nucleus and basal process of the basally positioned daughter cell that is known to undergo self-renewal. In con-

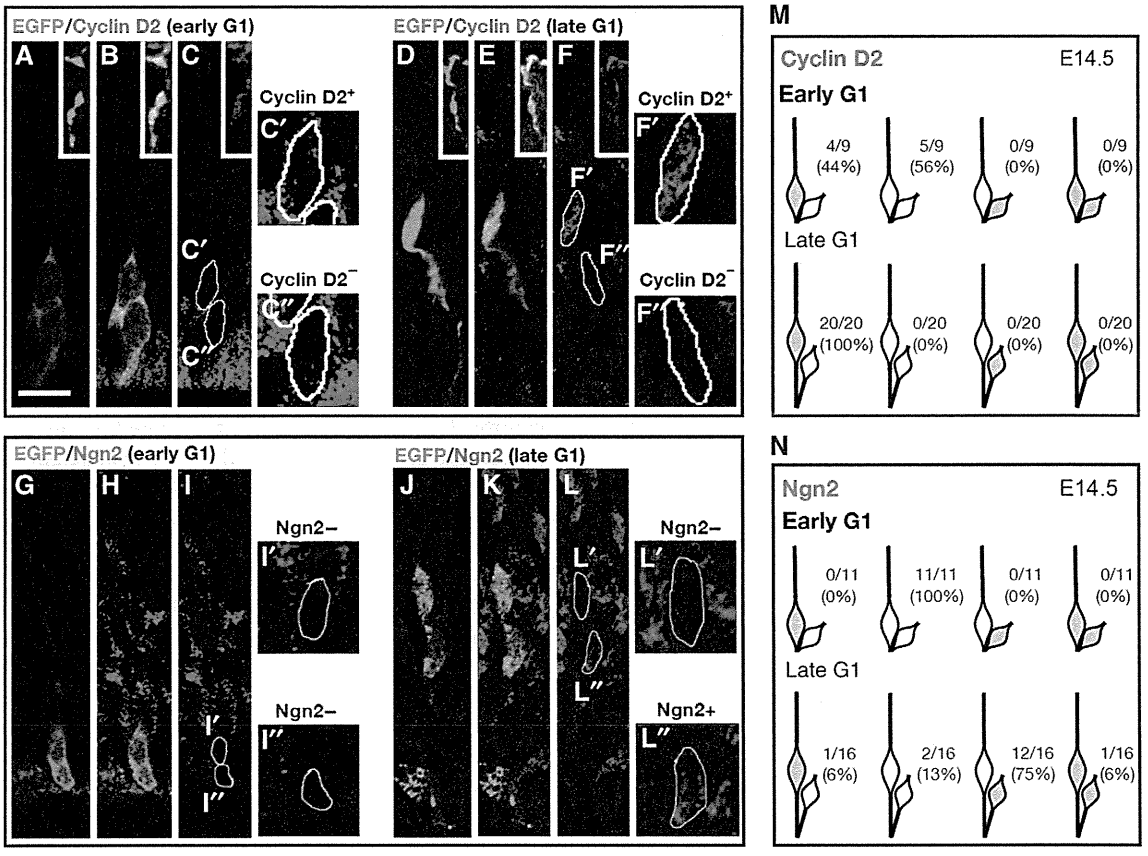

Figure 5 Cyclin D2 protein is asymmetrically inherited by basally positioned daughter cells. (**A–C''**) Daughter pairs at early G1 (<3 h after mitosis) labelled by EGFP lentivirus at E12.5 and examined at E14.5, inset in (**A–F**) shows Cyclin D2-positive basal process of radial glia. Higher magnification images (**C'** and **C''**) showing preferential allocation of Cyclin D2 to the basally positioned daughter (**C'**) while the apically positioned daughter (**C''**) is relatively empty of Cyclin D2. Strong expression of Cyclin D2 at the apical side indicates the process of other radial glial cells. (**G–I''**) At early G1 stage of the cell cycle, Ngn2 was not found in either of the two daughter cells (**I'** and **I''**). (**D–F''**) At late G1 (>3 h after mitosis), daughter pairs positioned next to the apical membrane show preferentially staining of Cyclin D2 in the basally positioned daughter cell (**F** and **F'**). In contrast, staining for the neuronal marker Ngn2 in a comparable cluster of late G1 daughters (**J–L''**) demonstrate that Ngn2 is preferentially expressed in the apically positioned daughter (**L** and **L''**). (**M**) Schematic diagram cataloguing the inheritance pattern of Cyclin D2 in late G1 (top row) and early G1 (bottom row). (**N**) Schematic diagram demonstrating Ngn2 expression in the apically positioned daughter cell in the majority (75%) of late G1 daughter pairs (top row). At early G1, Ngn2 marker is undetectable in either of the daughter cells (bottom row). Scale bar: 10 μm.

trast, by late G1 Cyclin D2 is invariably absent from the apically position daughter cell; these daughter cells acquire Ngn2 in most instances indicating terminal differentiation.

To discount the possibility that asymmetric Cyclin D2 distribution may have arisen from other causes apart from inheritance of locally translated mRNA, two further experiments were performed. The first experiment was to exclude that Cyclin D2 protein may have congregated to one side of the nucleus during M phase, resulting in subsequent asymmetry following division. To check this possibility, E14.5 M-phase neural progenitor cells were double stained with anti-pVim and anti-Cyclin D2 antibodies. The results show that Cyclin D2 protein was only weakly expressed in the nucleus during M phase, and in no case was the distribution asymmetric ($n=32$) (Supplementary Figure S6A–C). The second possibility is that one of the daughter cells committed for self-renewability may transcribe and translate Cyclin D2 *de novo*. If this is the case, then one of the two daughter cells should exhibit a higher level of *Cyclin D2* mRNA. This was not seen in daughter cells labelled with lentiviral infection and stained for *Cyclin D2* mRNA by *in-situ* hybridization (Supplementary Figure S6D–F', $n=6$). Instead, strong expression of *Cyclin D2* mRNA was observed at the basal endfeet of the basally positioned daughter cell (Supplementary Figure S6F). As a control, *Ngn2* mRNA showed clear asymmetry between daughter cells and was more intense in the apically positioned daughter cell (Supplementary Figure S6G–I').

Disruption of Cyclin D2 asymmetry by acute overexpression or knockdown of gene expression distorts progenitor cell fate

If asymmetrical partitioning of Cyclin D2 protein among mitotic descendants is important for determining cell fate, then systemic alterations of Cyclin D2 levels in neuronal progenitor cells should be expected to disturb the output of asymmetric cell divisions. This would lead to distortions in the ratios of APs, IPs, and differentiated neurons. To induce overexpression of Cyclin D2, *pCAX-Cyclin D2-ORF* (or control *pCAX*) was constructed and electroporated *in utero* at E13.5 together with *pCAX-EGFP-NLS* (to visualize the nucleus). To knockdown Cyclin D2, *si1726* or control siRNA was introduced into the E13.5 forebrain by *in-utero* electroporation together with *pCAX-EGFP* (Supplementary Figure S7A). Overexpression of Cyclin D2 (detectable as increased levels of mRNA and protein of Cyclin D2) in the VZ was clearly visible 24 h later in the vast majority of cells ($93.9\pm0.7\%$) present in the germinal zones ($n=3$) (Supplementary Figure S7C, G and J). In comparison, cortices ($n=3$) electroporated with control plasmid *pCAX* exhibited Cyclin D2 mRNA and protein in a smaller proportion of cells ($53.7\pm4.1\%$), representing endogenous levels of Cyclin D2 (Supplementary Figure S7B, F, and J; $P=0.000346$). Conversely, knockdown of endogenous Cyclin D2 using *si1726* produced a reduced number of Cyclin D2 immunopositive cells that was correlated with reduced *Cyclin D2* mRNA ($14\pm1.3\%$) (Supplementary Figure S7E, I, and J; $n=3$). It is of note that Cyclin D2 mRNA and protein were diminished from the basal endfeet (Supplementary Figure S7E and inset of Supplementary Figure S7I). As expected, control siRNA electroporated into forebrains ($n=3$) gave a similar proportion ($57.2\pm1.3\%$) of endogenously expressing Cyclin D2-positive cells and mRNA expression levels as *pCAX* control (Supplementary Figure S7D, H and J; $P=0.0000147$). We conclude that perturbing Cyclin D2, by overexpression or siRNA knockdown, is capable of disrupting the balance of Cyclin D2 leading to altered fates among daughter cells.

If differential Cyclin D2 levels in mitotic offspring can bias a cell towards a proliferative versus a differentiative fate, then altering Cyclin D2 levels on a global basis will be expected to change global ratios of cells with capacity for self-renewal (AP), further cell division but not renewal (IP), or fully differentiated (postmitotic neuron). Using markers to distinguish between these different cell types that coexist in the neuroepithelial wall, we quantified their relative frequency among EGFP-labelled cells that have become APs (Sox2+/Tbr2−), or IPs (Tbr2+), or differentiated neurons (SOX2−/Tbr2−) 24 h later (Supplementary Figure S7K–N). The results demonstrate that global overexpression of Cyclin D2 reduced the percentage of non-APs (marked by Tbr2+ or SOX2−/Tbr2− immunostaining) ($53.1\pm1.7\%$ compared with $57.2\pm1.2\%$ in the control; $P=0.0527$), but while at the same time increasing the percentage of APs (marked by SOX2+/Tbr2− staining) ($46.9\pm1.4\%$ compared with $42.6\pm1\%$ in the control; $P=0.0527$) (Supplementary Figure S7O). On the other hand, loss-of-function experiment by RNAi knockdown led to increased percentage of neuronal cells (marked by Tbr2+ or SOX2−/Tbr2− immunostaining) ($63.9\pm0.4\%$ compared with $56.9\pm1.4\%$ in the control; $P=0.01064$) at the expense of APs (SOX2+/Tbr2− immunostaining) ($36.1\pm0.4\%$ compared with $43.1\pm1.4\%$ in the control; $P=0.01064$) (Supplementary Figure S7O). Thus, widespread expression of Cyclin D2 leads to the increased frequency of AP fates.

To further examine how cell fate was affected by perturbation of Cyclin D2 asymmetry in the longer term, the gain/loss of Cyclin D2 was performed at E12.5, and the location of the EGFP-reporter cells was analysed 48 h after *in-utero* electroporation. We found that overexpression of Cyclin D2 dramatically decreases in the percentage of EGFP+ cells localized to the CP ($7.3\pm0.3\%$ compared with $15.3\pm0.2\%$ in the control; $P=0.01069$), while at the same time increasing the percentage of EGFP+ cells in the intermediate zone (IZ) and SVZ ($46.9\pm7.4\%$ compared with $37\pm0.7\%$ in the control; $P=0.0541$) (Figure 6A, B, and E). In the loss-of-function experiment, the percentage of EGFP+ cells localized to the CP was proportionally increased ($22.3\pm2.6\%$ compared with $15.4\pm0.3\%$ in the control; $P=0.0519$) at the expense of the percentages in the VZ ($18\pm0.7\%$ compared with $20.2\pm1\%$ in the control; $P=0.0535$) and SVZ ($18\pm2.7\%$ compared with $23.6\pm0.5\%$ in the control; $P=0.0534$) (Figure 6C–E). Therefore, disruption of asymmetrical localization of Cyclin D2 perturbed normal differentiation of neural progenitor cells, while overexpression inhibited neuronal differentiation, loss-of-function promoted neuronal differentiation.

To confirm whether Cyclin D2 conversely promotes cell proliferation, BrdU was pulse labelled for 15 min before sampling. Compared with controls, a larger number of BrdU-labelled cells and mitotic marker PHH3-positive cells were present in the VZ of samples overexpressing Cyclin D2 (Supplementary Figure S8A, B, E, and F), indicating hyperproliferation of neural progenitor cells. Furthermore, ectopic BrdU-labelled cells and PHH3-positive cells were observed in the SVZ and IZ when *Cyclin D2* was overexpressed, implying that intermediate progenitors and subventricular radial

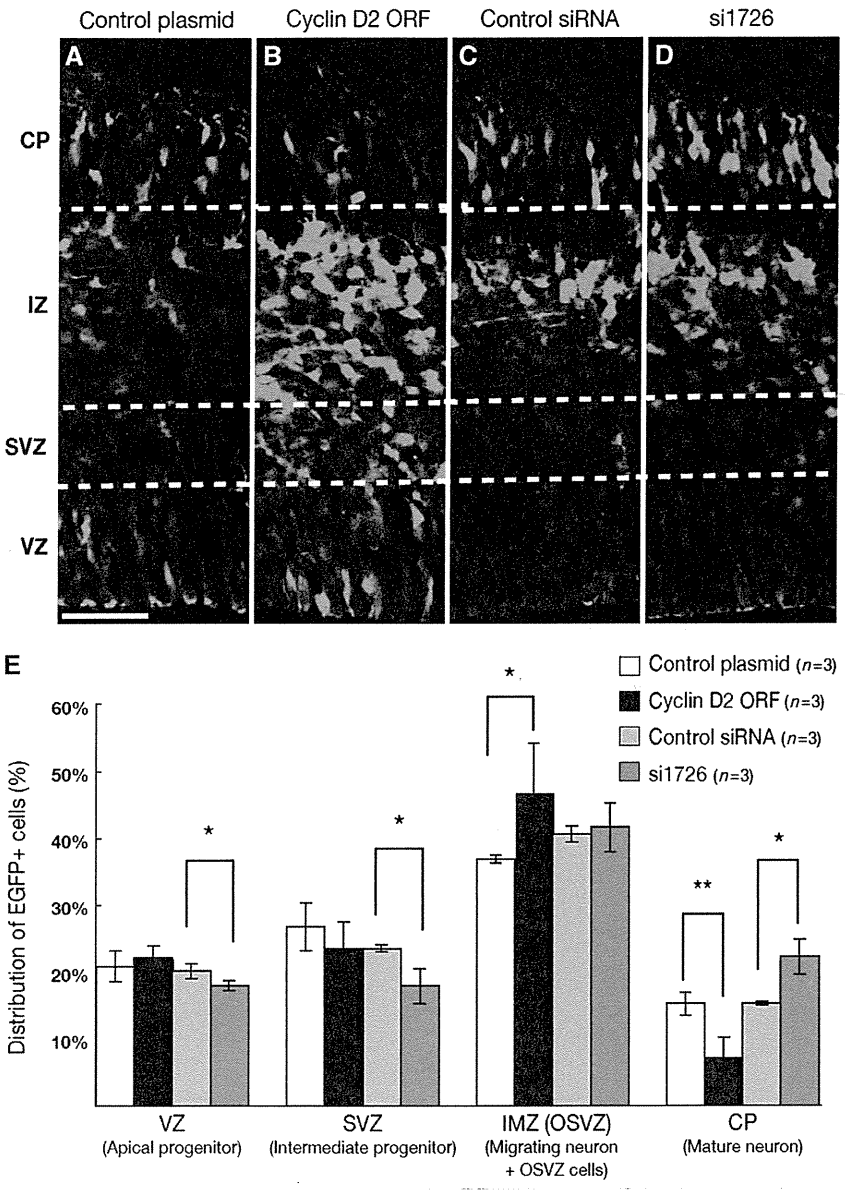

Figure 6 Alterations in cell position resulting from gain/loss of Cyclin D2. Cyclin D2 localization in cells expressing EGFP, 48 h after *in-utero* electroporation at E12.5 with control plasmid (*pCAX*), *pCAX-Cyclin D2-ORF*, control Stealth RNAi and Stealth RNAi for mouse *Cyclin D2* (si1726) together with *pCAX-EGFP*. Few EGFP + cells are observed in the CP of *pCAX-Cyclin D2-ORF*-electroporated samples (**B**) compared with control (**A**). In contrast, more EGFP + cells are observed in si1726-electroporated samples (**D**) than in controls (**C**) at CP. (**E**) Percentage of EGFP + cells in the ventricular zone (VZ), subventricular zone (SVZ) and intermediate zone/outer subventricular zone (IMZ/OSVZ) and cortical plate (CP). The VZ is identified as a Tbr2-negative zone and the SVZ identified as a Tbr2-positive zone (data not shown). IZ and CP were distinguished by their morphologies. Error bars indicate s.e.m. $*P<0.05$, $**P<0.01$, Student's *t*-test. Scale bar: 50 μm.

progenitors may undergone division in response to Cyclin D2 overexpression (Supplementary Figure S8A, B, E, and F). In contrast, downregulation of *Cyclin D2* dramatically decreased the number of BrdU-labelled cells and PHH3-positive cells in the VZ and the SVZ relative to controls (Supplementary Figure S8C, D, G, and H). These results confirm that Cyclin D2 is a very strong mitotic cue for neural progenitors.

We have demonstrated the inversely correlated expression patterns of Cyclin D2 and Ngn2 between daughter cells during cortical development (Figures 4N, 5M and N; Supplementary Figure S5). Moreover, the results obtained here revealed that loss of Cyclin D2 expression in the basally positioned daughter cells induced precocious neuronal differentiation (Figure 6E; Supplementary Figure S7O). Thus, all these findings consistently suggest the importance of the asymmetrical distribution of Cyclin D2 protein in the AP cell; specifically, Cyclin D2-negative apical daughter cells will differentiate into neurons, while Cyclin D2-positive basally positioned daughter cells will take on a progenitor fate and proceed to cell division.

Cyclin D2 expression in the developing human cortex

If asymmetric Cyclin D2 partitioning to mitotic offspring is crucial for the determination of self-renewing fate, then one would expect this mechanism to be both ancient and conserved. Since it is not feasible to perform similar perturbation

experiments on human brains, we decided to compare Cyclin D2 protein localization in the human cortex. At 16 and 19 gestational weeks (GW), Cyclin D2 protein was strongly observed at the marginal zone (MZ) and upper part of CP (Figure 7A–C). Cyclin D2 protein was not localized in the nuclei of CP cells, but localized in the basal endfoot of the radial glia in upper CP and MZ (Figure 7C–C''). In the relatively expanded subplate (SP) of the human cortex, punctate Cyclin D2 localization was observed along the glial fibres (Figure 7D–D''). In the VZ and inner SVZ (ISVZ), Cyclin D2 expression was observed in the nucleus of radial glia (Figure 7E–E''). Therefore, the general pattern of Cyclin D2 in humans is remarkably similar to the rodent, suggesting the conservation of this mechanism. Moreover, recent studies have identified new sub-populations of proliferative cells in the outer SVZ in the fetal human and ferret brains; these cells are distinguished by their possession of basal but not apical processes (Fietz *et al*, 2010; Hansen *et al*, 2010). Examination of cortical tissue at 19 GW confirmed that Cyclin D2 was present in cells of the OSVZ, and in addition, also present in the basal process (Figure 7F–H, insets). At the genetic level, it is noteworthy that human *Cyclin D2* mRNA (NM-001759) also contains a predicted 50 bp transport element in the 3′UTR (with 74% sequence match to the mouse), raising the possibility that basal transport of human *Cyclin D2* mRNA for local translation in the basal process may also be operative.

Discussion

During corticogenesis, the cells that populate the expanding cortical wall comprise a heterogeneous mixture of dividing and non-dividing cells. This balance is necessary to ensure that the correct number of neurons are generated at an appropriate stage, and at the same time, maintaining a pool of self-renewing progenitors. To achieve this, progenitors

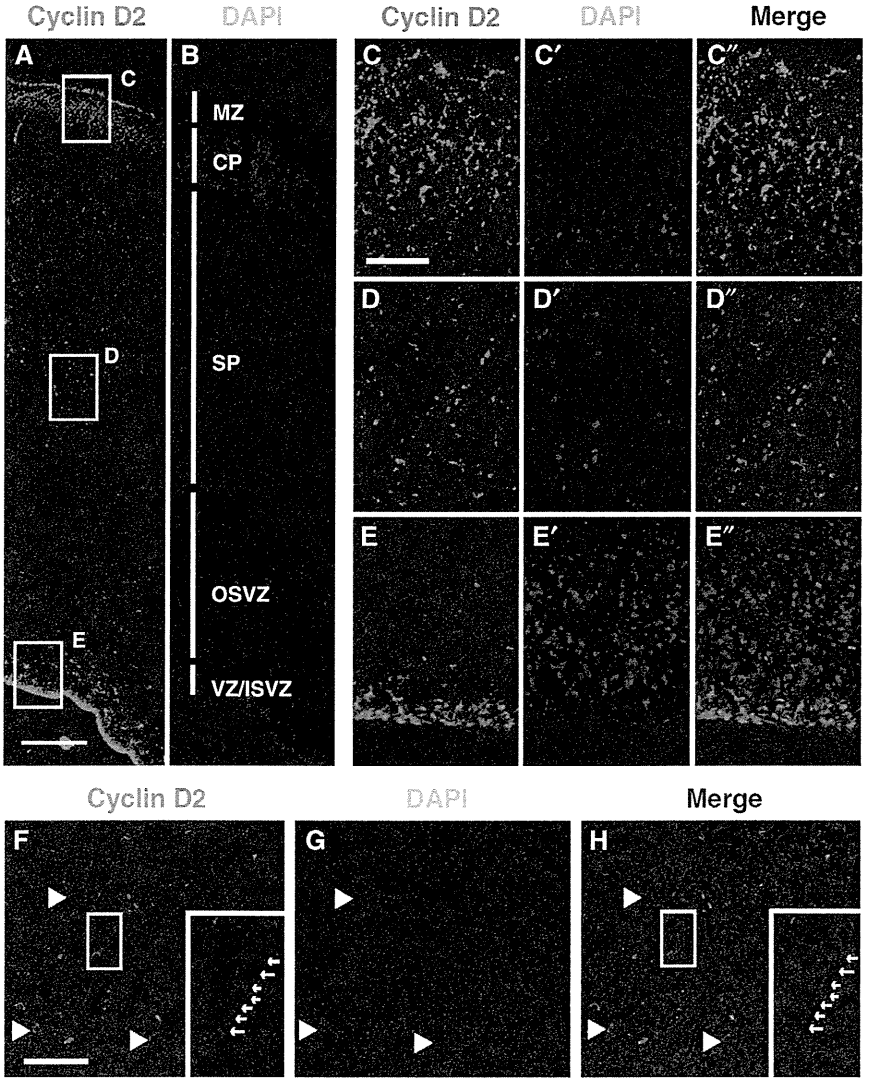

Figure 7 Cyclin D2 protein is expressed in the developing human cortex. (**A–E''**) At 16 GW, Cyclin D2 is expressed at three principal locations: the basal aspects of the CP near the MZ (box C); the subplate (box D), and the apical aspects of the VZ (box E). At higher magnification, Cyclin D2 in the basal aspects and the subplate are present in a punctate fashion along the cellular processes and not in the cell nuclei stained with DAPI (**C**, **D**). In the VZ, Cyclin D2 staining colocalizes with nuclei of neural progenitor cells (**E**). (**F–H**) Localization of Cyclin D2 protein in SP and OSVZ regions of the 19 GW human cortex showing Cyclin D2 staining in cells and also in a long basal process (**F** and **H**; arrows in insets). MZ, marginal zone; CP, cortical plate; SP, subplate; OSVZ, outer subventricular zone; VZ/ISVZ, ventricular zone/inner subventricular zone. Scale bars: 100 μm in (**A** and **B**), 25 μm in (**C–E''**), and 50 μm in (**F–H**).

undergo both symmetric and asymmetric cell divisions, but these events are classified by their outcomes rather than by their prior appearance or behaviour. While it is still not possible to forecast whether a progenitor will undergo symmetric or asymmetric division, a number of studies have attempted to link the mode of division with the acquisition of certain cellular and molecular characteristics. For example, cleavage plane orientation has been suggested to be a key factor (Chenn and McConnell, 1995; Zhong *et al*, 1996), but the low frequency of horizontal cleavage planes in the proliferative wall is irreconcilable with the large number of cortical neurons that needs to be produced (Huttner and Brand, 1997). While cleavage plane orientation is now considered to be unrelated to the mode of cell division (Attardo *et al*, 2008; Noctor *et al*, 2008), fate determinants such as Numb, present at the apical border, and TRIM32, present at the basal side of the cell body, appear to be preferentially inherited by the terminally differentiating daughter (Shen *et al*, 2002; Schwamborn *et al*, 2009). Other proteins found at the apical membrane, such as the Par complex (Costa *et al*, 2008; Bultje *et al*, 2009), have been implicated for controlling the balance between self-renewing and non-self-renewing divisions. By contrast, proteins enriched at the basal end of the progenitor have been less well studied as potential regulators of asymmetric versus symmetric cell division.

In this study, we revealed that allocation of Cyclin D2 to the tip of the basal process and its subsequent inheritance to the basally positioned daughter cell is strongly associated with the acquisition of a self-renewing fate of the AP. During mitosis the apically positioned daughter cell, expressing Ngn2, will adopt a different fate as a neuron or an IP (Figure 8). In summary, Cyclin D2 is expressed in the basal endfoot and nucleus, but by G1, it begins to be partitioned from the inherited basal process to the self-renewing daughter cell of the AP during an asymmetric division event. By late G1, asymmetric partitioning of Cyclin D2 becomes a hallmark for the basally positioned progenitor that is invariably non-neuronal (Ngn2 negative). Despite the first sign of Cyclin D2 asymmetry appearing in G1 pairs still attached to the apical surface, the majority of such daughter pairs either show equally weak Cyclin D2 distribution, or no Cyclin D2 whatsoever in both daughters. Interestingly, these daughter pairs rarely stain with Ngn2, suggesting the fate of each daughter cells remained uncommitted in this period.

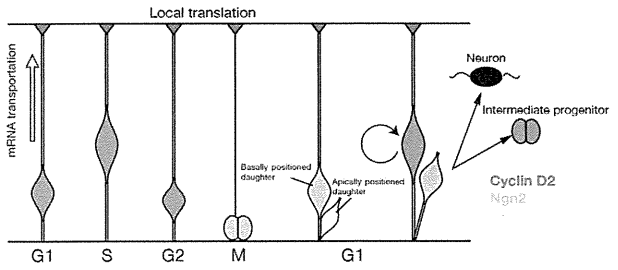

Figure 8 Schematic depiction of *Cyclin D2* mRNA and protein localization during the cell cycle and its putative role as a fate determinant. Pink and blue colours indicate Cyclin D2 and Ngn2 localization in the radial glia, respectively. *Cyclin D2* mRNA is transported to the basal endfoot during S-to-G2 phase (light pink arrow) and translated into protein. During mitosis, *Cyclin D2* mRNA or protein is inherited by the basally positioned daughter cell that assumes an apical progenitor fate.

If asymmetric distribution of Cyclin D2 is required for asymmetric cell fate determination, then Cyclin D2 overexpression should increase the frequency of symmetric cell divisions leading to increased numbers of APs, with concomitant reductions in numbers of differentiated neurons. These effects were observed with Cyclin D2 overexpression, and the opposite results obtained using RNAi knockdown experiments (Supplementary Figure S7O). Notably, this knockdown almost depleted mRNA and protein of Cyclin D2 from the endfeet, and produced a greater impact on the cell fate of neural progenitors compared with overexpression experiments. In summary, localization of Cyclin D2 in the basal endfoot has a critical role in the process of early corticogenesis.

An interesting aspect of Cyclin D2 is the strategy employed for unequal inheritance. Unlike Numb where the protein is preferentially allocated to the neuronal daughter (Shen *et al*, 2002), Cyclin D2 relies on transport of its mRNA during the S-to-G2 phase to the basal endfoot, where it is locally translated. This strategy relies on a 50-bp *cis*-acting transport element, present in full-length transcripts of *Cyclin D2* for translation into a 32-kDa protein (Denicourt *et al*, 2003), which is both necessary and sufficient for basal transport of fluorescent reporters. Importantly, this unique element is neither present in mouse *Cyclin D1* (Supplementary Figure S2) nor in chick *Cyclin D2* (NM-204213), both of which do not show asymmetric expression patterns in the developing forebrain. Sequence analysis of small RNAs do not exclude the possibility (Wang, 2008; Wang and El Naqa, 2008) that Cyclin D2 could be a potential target of certain microRNAs (e.g., mir-1192 and mir-495), but it remains unknown whether miRNA activity can be spatially distinctive enough to cause unequal distribution of *Cyclin D2* mRNA and protein in the endfoot. Moreover, a clear difference in Cyclin D2 protein levels between daughter cells is produced after cell division.

It has been mooted that inheritance of the basal process is associated with, and required for, asymmetric divisions (Konno *et al*, 2008). If that is correct, what then might be the mechanism that leads Cyclin D2 in the basal process to favour an AP fate? One possibility is that the long basal process increases the temporal interval for Cyclin D2 in the endfoot to gain access to the nucleus at G1. It is known that neural progenitors elongate their G1 phases during corticogenesis (Takahashi *et al*, 1995) and that progenitors at G1 are vulnerable to fate-determining events (McConnell and Kaznowski, 1991). Thus, delaying the interval of exposure to the nucleus by fate determinants such as Cyclin D2 may generate effects that are akin to shortening the G1 phase, thereby preventing the recipient nucleus from assuming a neuronal fate and favouring an AP fate. Indeed, artificial elongation of the G1 phase by another family protein, Cyclin D1, causes premature neurogenesis (Calegari and Huttner, 2003), while removal of Cyclin D2 gene by deletion causes G1 lengthening, leading to early exit from the cell cycle and encouraging neuronal differentiation (Glickstein *et al*, 2009). In that study, *Cyclin D2* knockout mice exhibit microcephaly and thinner cortical walls (Glickstein *et al*, 2009), features consistent with the present hypothesis that Cyclin D2 is crucial for maintaining divisions of APs.

In the present study, the increased focus on the basal process for AP fate has parallels in primates. In the outer

SVZ of human, ferret, and mouse cortices, a new population of proliferative cells have recently been reported to have basal processes but not apical processes and divide asymmetrically to produce one progenitor and one neuronal cell (Fietz *et al*, 2010; Hansen *et al*, 2010; Reillo *et al*, 2010; Wang *et al*, 2011). In addition, it has been reported that the basal process is instrumental for relaying a retinoic acid signal from the meninges to control progenitor cell proliferation (Siegenthaler *et al*, 2009). Given that we observe broad similarities in Cyclin D2 protein expression between developing mouse and human cortices, it is worth postulating that despite 70 million years of evolutionary divergence, the role of Cyclin D2 in maintaining AP renewal may be operative in all mammalian species. Furthermore, given its capacity to influence progenitor cell renewal, Cyclin D2 lends itself for evolutionary selection to increase the number of cell cycles (known to occur in primates) for generating a larger cortex (Finlay and Darlington, 1995; Rakic, 1995; Dehay and Kennedy, 2007), or within a given area of the cortex to generate more neurons for increased architectonic complexity (Dehay *et al*, 1993).

Materials and methods

Animals

Animal experiments were carried out in accordance with the National Institutes of Health Guide for the Care and Use of Laboratory Animals. The Committee for Animal Experimentation of the Tohoku University Graduate School of Medicine approved the experimental procedures described herein. The midday of the vaginal plug was designated as embryonic day 0.5 (E0.5). Pregnant ICR mice were purchased from Charles River Japan (Yokohama, Japan). *Cyclin D2* knockout mice were kindly obtained from Dr Sicinski (Sicinski *et al*, 1996).

Fetal tissue collection

Human fetal brain tissue was obtained from the NSW Fetal Tissue Consortium with approval from the University of Sydney Human Research Ethics Committee and the Melbourne Health Human Research Ethics Committee. This work was carried out under the NHMRC National Statement on Ethical Conduct in human research. Gestation age of fetus ranged between 16 and 19 weeks. Brain tissue was dissected and transported in ice-cold HEPES-buffered MEM (Invitrogen, Carlsbad, CA) and fixed in 4% paraformaldehyde (PFA) (w/v) in 0.1 M phosphate buffer (PB) for 1–9 h at 4°C. Fixed tissue was dehydrated in 20% sucrose in PB, embedded and frozen at −80°C in O.C.T compound (Tissue-Tek) and cryosectioned.

Staining procedures

In-situ hybridization and immunostaining procedures were performed according to methods previously described (Takahashi and Osumi, 2002). Antibodies used are listed in Supplementary Table 1. Information about probes, primers, and antibodies are supplied in Supplementary data.

Expression constructs

All expression constructs used in this study were cloned in frame into *pCAX* expression vector, a modified version of *pCAGGS*, in which multicloning site was inserted and the SV40 origin was deleted (kindly provided by the late K Umesono). All constructs were verified by sequence analysis. The entire mouse *Cyclin D2* cDNA (RIKEN MOUSE FANTOM, GenBank accession number AK14745) was obtained from DANAFORM (Yokohama, Japan). For the *cis*-acting transport element assay, parts of the *Cyclin* D2 3′UTR sequence were subcloned into *pCAX-EGFP* downstream of the EGFP sequence.

Gene transfer into mouse embryos by electroporation

The experimental procedures for whole-embryo culture and electroporation have been described previously (Osumi and Inoue, 2001; Takahashi *et al*, 2008). The *pCAGGS-mRFP* vector was kindly provided by Dr Masanori Uchikawa. The *pCAX-Cyclin D2-ORF* was generated by the insertion of PCR-amplified ORF into the *pCAX* vector. The stealth RNAi against mouse *Cyclin D2* (*Si1726*, UUAGGUAGCAGCUACUUUAGUCAGC) and the scramble control RNAi (*SiCtr*, UUACUGGAUGCGACUCAUGAUUAGC) were purchased from Invitrogen and used in 200 μg/μl phosphate buffer saline (PBS) solution.

Virus production and injection into the brain

EGFP lentivirus was produced using *pCS-EF-EGFP*, *pCMV-VSV-G-RSV-Rev*, and *pCAG-HIVgp* plasmids, which were kindly provided by Dr Miyoshi as described previously (Tahara-Hanaoka *et al*, 2002). For details, see Supplementary data.

Statistical analysis

The quantitative data were evaluated by Student's *t*-test, using Excel 2004 for Mac (Microsoft, WA, USA), and presented as mean ± s.e.m.

Supplementary data

Supplementary data are available at *The EMBO Journal* Online (http://www.embojournal.org).

Acknowledgements

We thank Drs Takaki Miyata and Yoichi Kosodo and Tadashi Nomura for a critical reading of the manuscript and valuable comments. We thank Drs Federico Calegari, Atsunori Shitamukai and Takashi Takeuchi for valuable suggestions on our work. We also thank Dr Hiroyuki Miyoshi for the lentivirus vectors, Dr Masanori Uchikawa for the *pCAGGS-mRFP* vector, and Dr Hiroto Okayama for rat *Cyclin D1* cDNA, Dr DJ Anderson for Ngn2 antibody, Dr Masato Nakafuku for Ngn2 probe, Dr Peter Sicinski for *Cyclin D2* knockout mouse. We are grateful to Ms Ayumi Ogasawara for animal care and Ms Sayaka Makino and Ms Makiko Sasaki-Hoshino for technical support. We thank all other members of the Osumi laboratory for their valuable discussions and hearty encouragement. The use of discarded human brain tissue was approved by Human Research Ethics Committee, Melbourne Health, Australia. This work was supported by KAKENHI (#17024001 to NO and #17700300 to MT) from MEXT, by CREST from the Japan Science and Technology Agency (JST) (to NO), the Global COE Program 'Basic and Translational Research Center for Global Brain Science' of MEXT of Japan (to NO), and by the Australian National Health and Medical Research Council. YT was supported by the GCOE program as a GCOE fellow.

Author contributions: YT, MT, and NO designed the experiments. MT designed and characterized the Ngn2 antibody, and YT carried out all other experiments except Figure 7, which was performed by JMB and S-ST. YT, JMB, MT, FP, S-ST, and NO discussed the results and wrote the manuscript. All authors read and approved the final manuscript.

Conflict of interest

The authors declare that they have no conflict of interest.

References

Alexandre P, Reugels AM, Barker D, Blanc E, Clarke JD (2010) Neurons derive from the more apical daughter in asymmetric divisions in the zebrafish neural tube. *Nat Neurosci* **13:** 673–679

Astrom KE, Webster HD (1991) The early development of the neopallial wall and area choroidea in fetal rats. A light and electron microscopic study. *Adv Anat Embryol Cell Biol* **123:** 1–76

Attardo A, Calegari F, Haubensak W, Wilsch-Brauninger M, Huttner WB (2008) Live imaging at the onset of cortical neurogenesis reveals differential appearance of the neuronal phenotype in apical versus basal progenitor progeny. *PLoS One* **3:** e2388

Bultje RS, Castaneda-Castellanos DR, Jan LY, Jan YN, Kriegstein AR, Shi SH (2009) Mammalian Par3 regulates progenitor cell asymmetric division via notch signaling in the developing neocortex. *Neuron* **63:** 189–202

Calegari F, Huttner WB (2003) An inhibition of cyclin-dependent kinases that lengthens, but does not arrest, neuroepithelial cell cycle induces premature neurogenesis. *J Cell Sci* **116**(Part 24): 4947–4955

Chenn A, McConnell SK (1995) Cleavage orientation and the asymmetric inheritance of Notch1 immunoreactivity in mammalian neurogenesis. *Cell* **82:** 631–641

Costa MR, Wen G, Lepier A, Schroeder T, Gotz M (2008) Par-complex proteins promote proliferative progenitor divisions in the developing mouse cerebral cortex. *Development* **135:** 11–22

Dehay C, Giroud P, Berland M, Smart I, Kennedy H (1993) Modulation of the cell cycle contributes to the parcellation of the primate visual cortex. *Nature* **366:** 464–466

Dehay C, Kennedy H (2007) Cell-cycle control and cortical development. *Nat Rev Neurosci* **8:** 438–450

Denicourt C, Kozak CA, Rassart E (2003) Gris1, a new common integration site in Graffi murine leukemia virus-induced leukemias: overexpression of a truncated cyclin D2 due to alternative splicing. *J Virol* **77:** 37–44

Fietz SA, Kelava I, Vogt J, Wilsch-Brauninger M, Stenzel D, Fish JL, Corbeil D, Riehn A, Distler W, Nitsch R, Huttner WB (2010) OSVZ progenitors of human and ferret neocortex are epithelial-like and expand by integrin signaling. *Nat Neurosci* **13:** 690–699

Finlay BL, Darlington RB (1995) Linked regularities in the development and evolution of mammalian brains. *Science* **268:** 1578–1584

Glickstein SB, Alexander S, Ross ME (2007) Differences in cyclin D2 and D1 protein expression distinguish forebrain progenitor subsets. *Cereb Cortex* **17:** 632–642

Glickstein SB, Monaghan JA, Koeller HB, Jones TK, Ross ME (2009) Cyclin D2 is critical for intermediate progenitor cell proliferation in the embryonic cortex. *J Neurosci* **29:** 9614–9624

Gotz M, Huttner WB (2005) The cell biology of neurogenesis. *Nat Rev* **6:** 777–788

Hansen DV, Lui JH, Parker PR, Kriegstein AR (2010) Neurogenic radial glia in the outer subventricular zone of human neocortex. *Nature* **464:** 554–561

Haubensak W, Attardo A, Denk W, Huttner WB (2004) Neurons arise in the basal neuroepithelium of the early mammalian telencephalon: a major site of neurogenesis. *Proc Natl Acad Sci USA* **101:** 3196–3201

Huttner WB, Brand M (1997) Asymmetric division and polarity of neuroepithelial cells. *Curr Opin Neurobiol* **7:** 29–39

Huttner WB, Kosodo Y (2005) Symmetric versus asymmetric cell division during neurogenesis in the developing vertebrate central nervous system. *Curr Opin Cell Biol* **17:** 648–657

Kamei Y, Inagaki N, Nishizawa M, Tsutsumi O, Taketani Y, Inagaki M (1998) Visualization of mitotic radial glial lineage cells in the developing rat brain by Cdc2 kinase-phosphorylated vimentin. *Glia* **23:** 191–199

Konno D, Shioi G, Shitamukai A, Mori A, Kiyonari H, Miyata T, Matsuzaki F (2008) Neuroepithelial progenitors undergo LGN-dependent planar divisions to maintain self-renewability during mammalian neurogenesis. *Nat Cell Biol* **10:** 93–101

Kosodo Y, Huttner WB (2009) Basal process and cell divisions of neural progenitors in the developing brain. *Dev Growth Differ* **51:** 251–261

Kosodo Y, Roper K, Haubensak W, Marzesco AM, Corbeil D, Huttner WB (2004) Asymmetric distribution of the apical plasma membrane during neurogenic divisions of mammalian neuroepithelial cells. *EMBO J* **23:** 2314–2324

Kosodo Y, Toida K, Dubreuil V, Alexandre P, Schenk J, Kiyokage E, Attardo A, Mora-Bermudez F, Arii T, Clarke JD, Huttner WB (2008) Cytokinesis of neuroepithelial cells can divide their basal process before anaphase. *EMBO J* **27:** 3151–3163

Kriegstein A, Noctor S, Martinez-Cerdeno V (2006) Patterns of neural stem and progenitor cell division may underlie evolutionary cortical expansion. *Nat Rev Neurosci* **7:** 883–890

Lange C, Huttner WB, Calegari F (2009) Cdk4/cyclinD1 overexpression in neural stem cells shortens G1, delays neurogenesis, and promotes the generation and expansion of basal progenitors. *Cell Stem Cell* **5:** 320–331

McConnell SK, Kaznowski CE (1991) Cell cycle dependence of laminar determination in developing neocortex. *Science* **254:** 282–285

Miyata T, Kawaguchi A, Okano H, Ogawa M (2001) Asymmetric inheritance of radial glial fibers by cortical neurons. *Neuron* **31:** 727–741

Miyata T, Kawaguchi A, Saito K, Kawano M, Muto T, Ogawa M (2004) Asymmetric production of surface-dividing and non-surface-dividing cortical progenitor cells. *Development* **131:** 3133–3145

Noctor SC, Flint AC, Weissman TA, Dammerman RS, Kriegstein AR (2001) Neurons derived from radial glial cells establish radial units in neocortex. *Nature* **409:** 714–720

Noctor SC, Martinez-Cerdeno V, Ivic L, Kriegstein AR (2004) Cortical neurons arise in symmetric and asymmetric division zones and migrate through specific phases. *Nat Neurosci* **7:** 136–144

Noctor SC, Martinez-Cerdeno V, Kriegstein AR (2008) Distinct behaviors of neural stem and progenitor cells underlie cortical neurogenesis. *J Comp Neurol* **508:** 28–44

Ochiai W, Nakatani S, Takahara T, Kainuma M, Masaoka M, Minobe S, Namihira M, Nakashima K, Sakakibara A, Ogawa M, Miyata T (2009) Periventricular notch activation and asymmetric Ngn2 and Tbr2 expression in pair-generated neocortical daughter cells. *Mol Cell Neurosci* **40:** 225–233

Osumi N, Inoue T (2001) Gene transfer into cultured mammalian embryos by electroporation. *Methods* **24:** 35–42

Palacios IM, St Johnston D (2001) Getting the message across: the intracellular localization of mRNAs in higher eukaryotes. *Annu Rev Cell Dev Biol* **17:** 569–614

Rakic P (1988) Specification of cerebral cortical areas. *Science* **241:** 170–176

Rakic P (1995) A small step for the cell, a giant leap for mankind: a hypothesis of neocortical expansion during evolution. *Trends Neurosci* **18:** 383–388

Reillo I, de Juan Romero C, Garcia-Cabezas MA, Borrell V (2010) A role for intermediate radial glia in the tangential expansion of the mammalian cerebral cortex. *Cereb Cortex* **21:** 1674–1694

Ross ME, Carter ML, Lee JH (1996) MN20, a D2 cyclin, is transiently expressed in selected neural populations during embryogenesis. *J Neurosci* **16:** 210–219

Salomoni P, Calegari F (2010) Cell cycle control of mammalian neural stem cells: putting a speed limit on G1. *Trends Cell Biol* **20:** 233–243

Schwamborn JC, Berezikov E, Knoblich JA (2009) The TRIM-NHL protein TRIM32 activates microRNAs and prevents self-renewal in mouse neural progenitors. *Cell* **136:** 913–925

Shen Q, Zhong W, Jan YN, Temple S (2002) Asymmetric Numb distribution is critical for asymmetric cell division of mouse cerebral cortical stem cells and neuroblasts. *Development* **129:** 4843–4853

Sicinski P, Donaher JL, Geng Y, Parker SB, Gardner H, Park MY, Robker RL, Richards JS, McGinnis LK, Biggers JD, Eppig JJ, Bronson RT, Elledge SJ, Weinberg RA (1996) Cyclin D2 is an FSH-responsive gene involved in gonadal cell proliferation and oncogenesis. *Nature* **384:** 470–474

Siegenthaler JA, Ashique AM, Zarbalis K, Patterson KP, Hecht JH, Kane MA, Folias AE, Choe Y, May SR, Kume T, Napoli JL, Peterson AS, Pleasure SJ (2009) Retinoic acid from the meninges regulates cortical neuron generation. *Cell* **139:** 597–609

Smart IH (1973) Proliferative characteristics of the ependymal layer during the early development of the mouse neocortex: a pilot study based on recording the number, location and plane of cleavage of mitotic figures. *J Anat* **116**(Part 1): 67–91

Tahara-Hanaoka S, Sudo K, Ema H, Miyoshi H, Nakauchi H (2002) Lentiviral vector-mediated transduction of murine CD34(-) hematopoietic stem cells. *Exp Hematol* **30:** 11–17

Takahashi M, Nomura T, Osumi N (2008) Transferring genes into cultured mammalian embryos by electroporation. *Dev Growth Differ* **50:** 485–497

Takahashi M, Osumi N (2002) Pax6 regulates specification of ventral neurone subtypes in the hindbrain by establishing progenitor domains. *Development* **129:** 1327–1338

Takahashi M, Sato K, Nomura T, Osumi N (2002) Manipulating gene expressions by electroporation in the developing brain of mammalian embryos. *Differentiation* **70:** 155–162

Takahashi T, Nowakowski RS, Caviness Jr VS (1995) The cell cycle of the pseudostratified ventricular epithelium of the embryonic murine cerebral wall. *J Neurosci* **15:** 6046–6057

Wang X (2008) miRDB: a microRNA target prediction and functional annotation database with a wiki interface. *RNA* **14:** 1012–1017

Wang X, El Naqa IM (2008) Prediction of both conserved and nonconserved microRNA targets in animals. *Bioinformatics* **24:** 325–332

Wang X, Tsai JW, LaMonica B, Kriegstein AR (2011) A new subtype of progenitor cell in the mouse embryonic neocortex. *Nat Neurosci* **14:** 555–561

Zhong W, Feder JN, Jiang MM, Jan LY, Jan YN (1996) Asymmetric localization of a mammalian numb homolog during mouse cortical neurogenesis. *Neuron* **17:** 43–53

International Orthopaedics (SICOT) (2012) 36:185–190
DOI 10.1007/s00264-011-1263-1

ORIGINAL PAPER

Comparison of articular cartilage images assessed by high-frequency ultrasound microscope and scanning acoustic microscope

Yoshihiro Hagiwara · Yoshifumi Saijo · Akira Ando · Yoshito Onoda · Hideaki Suda · Eiichi Chimoto · Kouki Hatori · Eiji Itoi

Received: 27 January 2011 / Accepted: 4 April 2011 / Published online: 13 May 2011

Abstract
Purpose The purpose of this study was to compare images of a newly developed high-frequency ultrasound imaging system (HFUIS) and scanning acoustic microscope (SAM) and to calculate their Pearson product moment correlations with a view to applying HFUIS for clinical use.
Methods Cylindrical cartilage–bone complexes from adult male Sprague-Dawley rats were obtained. The specimens were immersed in normal saline and scanned by HFUIS. Intensity by HFUIS was normalised by reflection from a steel plate at the same distance. After the scanning, specimens were fixed with paraformaldehyde, decalcified and embedded in paraffin. Thinly sliced tissues were prepared for SAM evaluation. After the scanning, three layers of articular cartilage (superficial, middle and deep) were independently evaluated and their relationships calculated.
Results The superficial and deep layers indicated high relative intensity, whereas the middle layer showed nonhomogeneous relative intensity by HFUIS. A high relative intensity by HFUIS and high sound speed area by SAM had strong correlations (Pearson product moment correlation, superficial layer 0.704, middle layer 0.731).
Conclusions HFUIS produced high-resolution images of the articular cartilage and its intensity was strongly correlated with sound speed by SAM.

Y. Hagiwara · A. Ando · Y. Onoda · H. Suda · E. Chimoto · E. Itoi
Department of Orthopaedic Surgery,
Tohoku University School of Medicine,
1-1 Seiryo-machi, Aoba-ku,
Sendai 980-8574, Japan

Y. Saijo (✉)
Department of Biomedical Imaging, Graduate School
of Biomedical Engineering, Tohoku University,
4-1 Seiryo-machi, Aoba-ku,
Sendai 980-8575, Japan
e-mail: saijo@idac.tohoku.ac.jp

K. Hatori
Division of Advanced Prosthetic Dentistry,
Tohoku University School of Dentistry,
4-1 Seiryo-machi, Aoba-ku,
Sendai 980-8575, Japan

Introduction

Articular cartilage is a viscoelastic connective tissue with a smooth surface, which serves as a cushion between joint bones. During mechanical loading, interstitial water flows out of the tissue to the joint space together with the synovial fluid, which guarantees almost frictionless motion between tangentially contacting joint surface [1]. Osteoarthritis (OA) is a common joint disorder and estimated to cause symptoms in 20–40% of the elderly population [2, 3]. Its symptoms are pain, joint stiffness and muscle weakness [4]. Intra-articular injection of hyaluronic acid and ingestion of glucosamine are suggested for treating early knee OA [5]. If conservative treatment fails, patients require surgical intervention such as total arthroplasty to relieve pain [6]. However, surgical implants are not permanent and need revision.

OA is characterised by collagen network disruption, proteoglycan depletion, water content increase and deterioration of mechanical properties of the articular cartilage [7]. Injury to the collagen network is thought to represent the point of no return in OA progression [8]. Because superficial cartilage degradation is the first sign of OA, its early detection would be of diagnostic importance [9]. Once the superficial layer of the articular

cartilage is damaged, its mechanical properties deteriorate and degenerative changes begin to accumulate. If the early change is properly diagnosed, disease progression may be slowed by medication or lifestyle changes [10]. Therefore, early detection of the pathological changes in the articular cartilage is essential in order to treat the disease successfully [1].

Modalities for diagnosing knee OA include noninvasive techniques such as plain X-rays, computed tomography (CT), magnetic resonance imaging (MRI) and ultrasonography (US); and invasive techniques such as arthrography and arthroscopy. MRI is a powerful tool for evaluating the articular cartilage, although location and economic limitation for routine use remain [6] and its resolution ability is not high. Arthroscopy is the only method by which to evaluate surface morphology and softness of the degenerated articular cartilage. However, it reveals only macroscopic changes and cannot be used repeatedly because of its invasiveness. US is quick and inexpensive, and its resolution higher than MRI. US plays an important role in assessing musculoskeletal soft tissues [11], articular cartilage and subchondral bone [9]. Though US is a skill-dependent method, there is a significant correlation between in vivo US and histological evaluation of the OA cartilage [12].

A scanning acoustic microscope (SAM) characterises biological tissues by estimating the elastic parameters based on sound speed with a central frequency of 80 MHz [13]. SAM allows visualisation of thinly sliced tissues [14, 15] or single-layered cultured cells [16]. In our previous study, articular cartilage degeneration induced by joint immobilisation demonstrated a decrease in sound speed [17]. Because preparation of sliced tissues is needed for SAM, it is not suitable for chronological evaluations. An intravascular US (IVUS) catheter is clinically approved for evaluating atherosclerosis and has the potential to evaluate articular cartilage [18] and subchondral bone, which are both involved in OA progression [19]. Surface roughness and articular cartilage integrity were quantitatively evaluated with IVUS and qualitative information on repaired tissues was assessed [18].

High-frequency US, signal-processing software and imaging technique advances in newer-generation acoustic microscopy allow imaging without thinly sliced tissues. The group lead by Foster et al. commercialised a high-frequency (40–60 MHz) B-mode imaging device as an ultrasound biomicroscope for animal experiments [20] and skin imaging [21]. HFUIS with a central frequency of 120 MHz provides noncontact high-resolution US impedance and 3D US imaging [22]. Articular cartilage softening is the initial sign of degeneration [9]. Intraoperative evaluation of the articular cartilage and lesion assessment are important in orthopaedic operations. The purpose of this study was to assess normal articular cartilage by HFUIS and SAM and calculate their correlations with the intention of applying HFUIS to IVUS systems.

Materials and methods

HFUIS

A schematic illustration of HFUIS is shown in Fig. 1. The system has been reported previously [22] and is

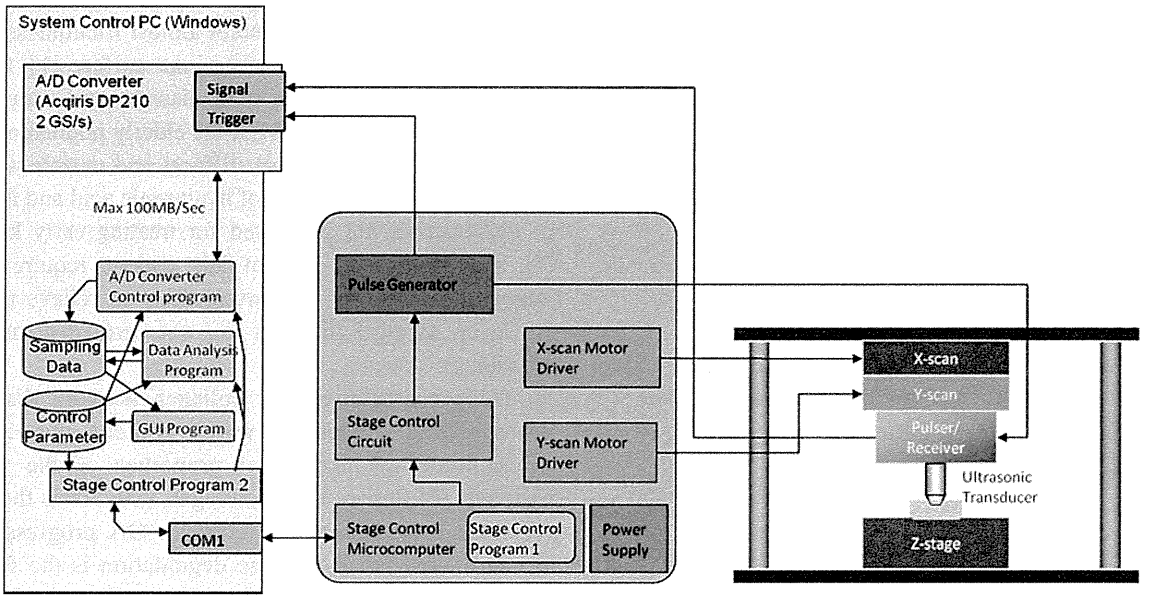

Fig. 1 High-frequency ultrasound imaging system

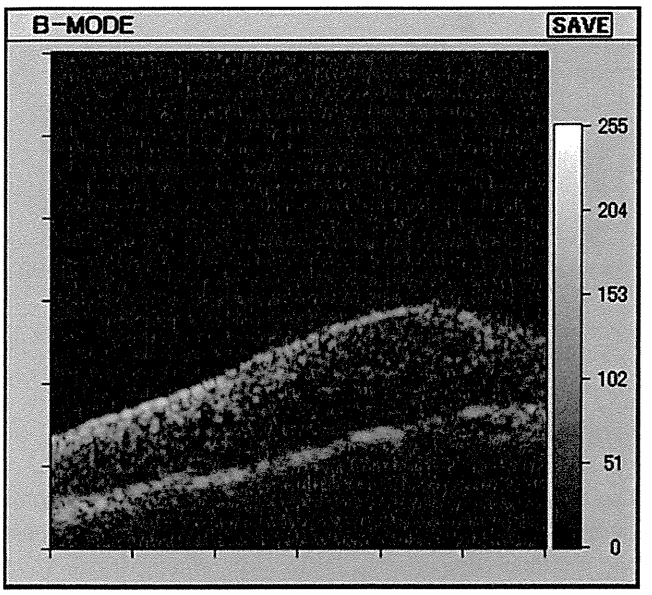

Fig. 2 High-frequency ultrasound imaging system (HFUIS) image of the articular cartilage clearly visualising three layers: superficial, middle and deep. The superficial and deep layers expressed high relative intensities

described briefly as follows. An electrical impulse is generated by a high-speed switching semiconductor. The electric pulse is used to excite a polyvinylidene fluoride (PVDF) transducer with a central frequency of 120 MHz and a focal length of 3.2 mm. HFUIS has three measurement modes: (1) conventional C-mode acoustic microscopic imaging of excised, thinly sliced tissue; (2) US impedance imaging of the tissue surface; (3) 3D US imaging visualising the inside of tissue. A 3D high-frequency US microscope creates conventional C- and B-mode images and 3D images reconstructed from B-mode images. Intensity was normalised by the reflection from a steel plate at the same distance.

SAM

The system used in this study has been reported elsewhere [14–17] and thus is briefly described as follows. Reflections from the tissue surface and from the interface between tissue and glass are received by the same transducer. The central frequency is 80 MHz. Frequency domain analysis of the reflection enables the separation of these two components and calculation of tissue thickness and intensity by Fourier transformation the waveform [13]. Normal light microscopic images corresponding to the stored acoustic images are captured (DMLB 100 HC light microscope; LEICA, Wetzlar, Germany). Relative intensity by HFUIS and sound speed of the articular cartilage by SAM are calculated with gray-scale images using commercially available image analysis software (PhotoShop CS2, Adobe Systems Inc., San Jose, CA, USA). SAM images with a gradation colour scale are also produced for clear sound-speed visualisation. Optical and acoustic images are compared to ensure morphological congruence in the analysis. The articular cartilage is divided into three layers (superficial, middle and deep) and analysed independently. We divided the articular cartilage—from the surface of to the margin of the high-intensity areas (subchondral bone) in HFUIS and high sound-speed areas (subchondral bone) in SAM—into five areas. We defined one fifth from the surface as superficial layers and the rest as middle layers.

Tissue preparation

The protocol for the experiments was approved by the Animal Research Committee of the Tohoku University School of Medicine. We used six adult male Sprague-Dawley rats (16 weeks). The knee capsule was cut with a surgical knife and the joint opened after administration of an overdose of sodium pentobarbital. After resection of ligaments and meniscus, a

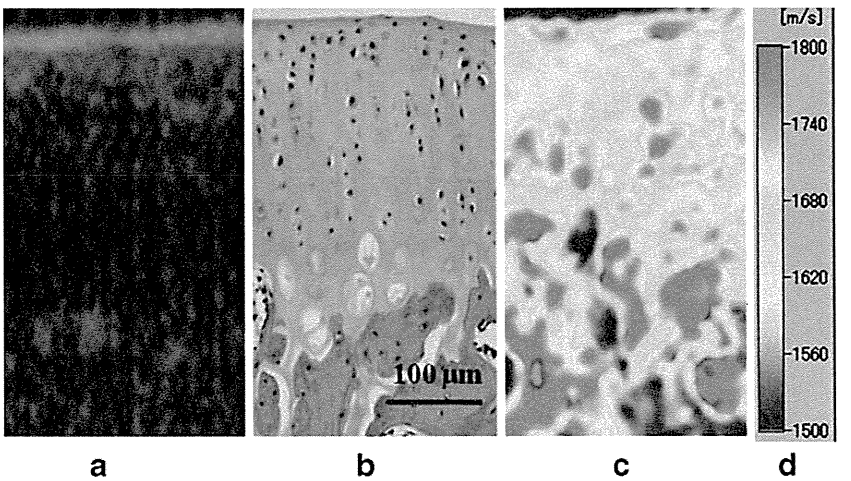

Fig. 3 Comparison of the articular cartilage images: **a** high-frequency ultrasound imaging system (HFUIS), **b**: haematoxylin and eosin stain, **c**scanning electron microscopy (SAM), **d** colour scale bar for SAM. Superficial layer indicates high relative intensity by HFUIS and corresponds well to that of high sound-speed area by SAM

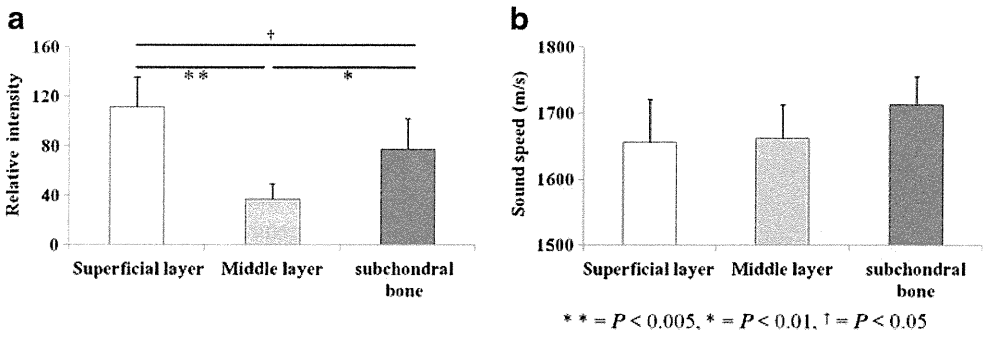

Fig. 4 Comparison of three layers of the articular cartilage: **a** high-frequency ultrasound imaging system (HFUIS), **b** scanning electron microscopy (SAM). Intensity of the superficial and deep layers was significantly higher than that of the middle layer by HFUIS. There was no statistical difference among the three layers by SAM

cartilage–bone complex (3.8 mm diameter) was obtained from the medial midcondylar regions of the tibia with a cylindrical bar (Trephine Bur, cat. No.13006, Technika Inc., Tokyo, Japan). Specimens were immediately immersed in saline at room temperature before scanning with HFUIS. After scanning, specimens were immersed in 4% paraformaldehyde in 0.1 M phosphate buffer, pH 7.4, overnight at 4°C. The fixed specimens were then decalcified in 10% ethylenediaminetetraacetate (EDTA) in 0.01 M phosphate buffer, pH 7.4, for one week at 4°C. After dehydration through a graded series of ethanol solutions, specimens were embedded in paraffin. The embedded tissue was cut into 5-μm sagittal sections from the medial to the lateral side of the joint, as in previous reports [15]. After deparaffinisation, the sections were assessed by SAM. Sections stained with haematoxylin and eosin (H&E) sections were used to ensure morphological congruence in the analysis.

Statistics

The three individual layers were analysed using one-factor analysis of variance (ANOVA) with Bonferroni/Dunn post hoc multiple comparisons. Differences among layers were analysed with a paired *t* test and expressed as mean±standard deviation (SD). Correlation coefficients were calculated by Pearson product moment correlation. $P<0.05$ was accepted as statistically significant.

Results

HFUIS clearly visualised three layers of articular cartilage (Fig. 2). The superficial and deep layers indicated high relative intensity. The middle layer gradually became low relative intensity from the articular cartilage surface. The

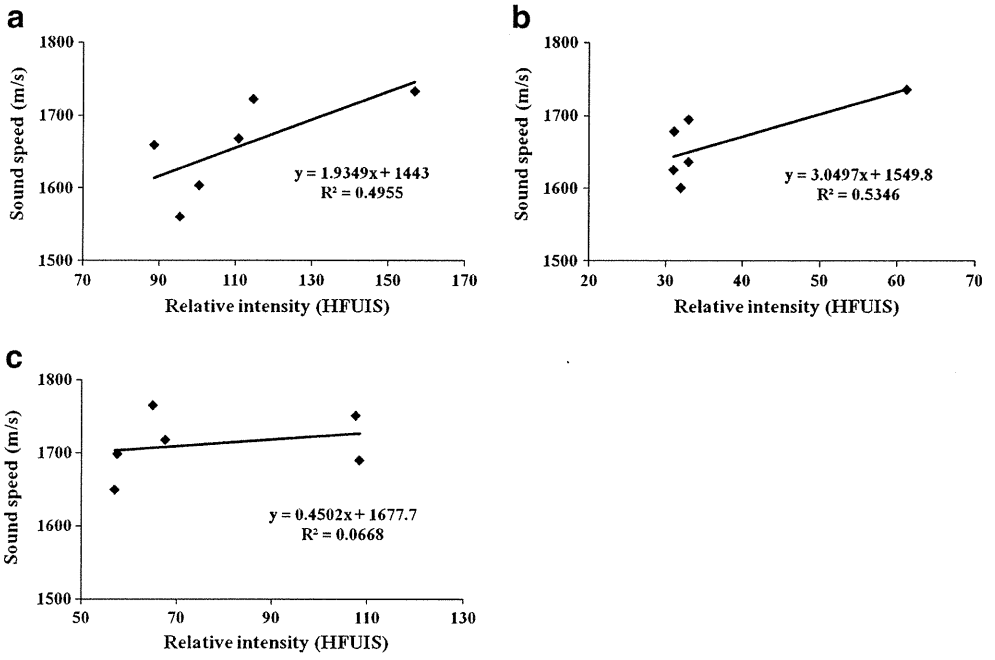

Fig. 5 Pearson product moment correlations of the three layers of the articular cartilage: **a** superficial layer, **b**: middle layer, **c** deep layer. Though the deep layer had low correlation, the superficial and middle layers had strong correlations between high-frequency ultrasound imaging system scanning electron microscopy

high signal-intensity areas by HFUIS corresponded well with high sound-speed areas by SAM; however, the middle layer did not (Fig. 3). Among the three layers, signal intensity of the middle layer by HFUIS was significantly lower than that of the other two layers (Fig. 4a). There was no statistically significant difference among the three layers of sound speed by SAM (Fig. 4b). In the superficial and middle layers, there were strong positive correlations between the relative intensity and sound speed (Pearson product moment correlation, superficial layer 0.704; middle layer 0.731) (Figs. 5a, b). There was a low positive correlation between them in the deep layer (Pearson product moment correlation 0.258) (Fig. 5c).

Discussion

The US feature of normal articular cartilage is a homogenous anechoic band with a sharp superficial cartilage profile and subchondral bone profile [6]. The lack of echoes is due to a uniform transmission of sound waves with high water content [23] and densely packed, regularly organised, collagen [24]. The major features of OA cartilage by US were loss of margin sharpness, loss of cartilage band clarity, and thickness reduction [24]. On US, higher spatial resolution is reached by increasing the frequency of the imaging system [25]. Because the central frequency is 120 MHz and spatial resolution is 15 μm [22], HFUIS clearly distinguished three layers of articular cartilage with high resolution compared with conventional high-frequency B-mode imaging modalities. Furthermore, it could clearly visualise the non-homogeneous middle layer of the articular cartilage. HFUIS has a potential to evaluate articular cartilage histology. SAM clearly visualised the mechanical property, based on sound speed, of the articular cartilage. In our previous report, articular cartilage degeneration induced by joint immobilisation demonstrated decrease in sound speed [17]. As SAM requires sliced tissues, it is not adaptable for in vivo real-time and sequential evaluations. However, it is a powerful tool for evaluating tissue elasticity and distribution in the targeted tissue in situ.

This study reports, for the first time, the Pearson product moment correlation of the articular cartilage between relative intensity by HFUIS and sound speed by SAM. The superficial and middle layer showed strong correlations; however, the deep layer showed a weak correlation. Because the deep layer profile might include the calcified zone and the subchondral bone, it was difficult to specify subchondral bone only by US. Further, decalcification might influence the mechanical property of the subchondral bone for SAM evaluation. For these reasons, the deep layer seemed to indicate weak correlations.

In clinical situations, applying HFUIS in a weight-bearing portion of the knee may be difficult because of the patella. Overlying soft tissues, such as synovitis with synovial fluid, may also influence echogenicity of articular cartilage [23, 24]. The earlier US features of OA are loss of cartilage-band clarity and margin sharpness [6]. As for OA articular cartilage histology, there was significant correlation between in vivo US histological grading [12]. Because of the softening, the early change in articular cartilage is only detectable by arthroscopic examinations. Therefore, HFUIS has a potential to detect early changes in articular cartilage besides its colour and morphology. Because the subchondral bone is also affected by OA progression, further study is needed to specify articular cartilage echogenicity and distinguish the subchondral bone by US [18].

Conclusions

HFUIS produced high-resolution images of the articular cartilage, and its intensity was strongly correlated with sound speed by SAM.

Acknowledgment This research was supported by the Ministry of Education, Science, Sports and Culture, Grant-in-Aid for Young Scientists (B).

References

1. Nieminen HJ, Julkunen P, Töyräs J, Jurvelin JS (2007) Ultrasound speed in articular cartilage under mechanical compression. Ultrasound Med Biol 11:1755–1766
2. Zhang YQ, Jordan JM (2008) Epidemiology of osteoarthritis. Rheum Dis Clin North Am 34:515–529
3. Felson DT (1988) Epidemiology of hip and knee osteoarthritis. Epidemiol Rev 10:1e–28e
4. O'Reilly SC, Jones A, Muir KR, Doherty M (1998) Quadriceps weakness in knee osteoarthritis: the effect on pain and disability. Ann Rheum Dis 57:588–594
5. Altman RD, Moskowitz R (1998) Intraarticular sodium hyaluronate (Hyalgan) in the treatment of patients with osteoarthritis of the knee: a randomized clinical trial. Hyalgan Study Group. J Rheumatol 25:2203–2212
6. Tsai CY, Lee CL, Chai CY, Chen CH, Su JY, Huang HT, Huang MH (2007) The validity of in vitro ultrasonographic grading of osteoarthritic femoral condylar cartilage–a comparison with histologic grading. Osteoarthritis Cartilage 15:245–250
7. Buckwalter JA, Mankin HJ (1998) Articular cartilage: degeneration and osteoarthritis, repair, regeneration, and transplantation. Instr Course Lect 47:487e–504e
8. Buckwalter JA, Mankin HJ (1997) Articular cartilage, part II: degeneration and osteoarthritis, repair regeneration, and transplantation. J Bone Joint Surg Am 79:600–611
9. Aula AS, Töyräs J, Tiitu V, Jurvelin JS (2010) Simultaneous ultrasound measurement of articular cartilage and subchondaral bone. Osteoarthritis Cartilage 18:1570–1576

10. Buckwalter JA, Martin J (1995) Degenrative joint disease. Clin Symp 47:1–32
11. Harcke HT, Grissom LE, Finkelstein MS (1988) Evaluation of the musculoskeletal system with sonography. AJR Am J Roentgenol 150:1253–1261
12. Lee CL, Huang MH, Chai CY, Chen CH, Su JY, Tien YC (2008) The validity of in vivo ultrasonographic grading of osteoarthritic femoral condylar cartilage: a comparison with in vitro ultrasonographic and histologic gradings. Osteoarthritis Cartilage 16:352–358
13. Hozumi N, Yamashita R, Lee CK, Nagao M, Kobayashi K, Saijo Y, Tanaka M, Tanaka N, Ohtsuki S (2004) Time-frequency analysis for pulse driven ultrasonic microscopy for biological tissue characterization. Ultrasonics 42:717–722
14. Saijo Y, Jorgensen S, Mondek P, Sefranek V, Paaske W (2002) Acoustic inhomogeneity of carotid arterial plaques determined by GHz frequency range microscopy. Ultrasound Med Biol 28:933–937
15. Hagiwara Y, Saijo Y, Chimoto E, Akita H, Sasano Y, Matsumoto F, Kokubun S (2006) Increased elasticity of capsule after immobilization in a rat knee experimental model assessed by scanning acoustic microscopy. Ups J Med Sci 111:303–313
16. Hagiwara Y, Saijo Y, Ando A, Chimoto E, Suda H, Onoda Y, Itoi E (2009) Ultrasonic intensity microscopy for imaging of living cells. Ultrasonics 49:386–388
17. Hagiwara Y, Ando A, Chimoto E, Saijo Y, Ohmori-Matsuda K, Itoi E (2009) Changes of articular cartilage after immobilization in a rat knee contracture model. J Orthop Res 27:236–242
18. Virén T, Saarakkala S, Jurvelin JS, Pulkkinen HJ, Tiitu V, Valonen P, Kiviranta I, Lammi MJ, Töyräs J (2010) Quantitative evaluation of spontaneously and surgically repaired rabbit articular cartilage using intra-articular ultrasound method in situ. Ultrasound Med Biol 36:833–839
19. Anderson-MacKenzie JM, Quasnichka HL, Starr RL, Lewis EJ, Billingham ME, Bailey AJ (2005) Fundamental subchondral bone changes in spontaneous knee osteoarthritis. Int J Biochem Cell Biol 37:224–236
20. Foster FS, Pavlin CJ, Harasiewicz KA, Christopher DA, Turnbull DH (2000) Advances in ultrasound biomicroscopy. Ultrasound Med Biol 26:1–27
21. Vogt M, Ermert H (2007) In vivo ultrasound biomicroscopy of skin: spectral system characteristics and inverse filtering optimization. IEEE Trans Ultrason Ferroelectr Freq Control 54:1551–1559
22. Saijo Y, Kobayashi K, Okada N, Hozumi N, Hagiwara Y, Tanaka A, Iwamoto T (2008) High frequency ultrasound imaging of surface and subsurface structures of fingerprints. Conf Proc IEEE Eng Med Biol Soc 2008:2173–2176
23. Grassi W, Lamanna G, Farina A, Cervini C (1999) Sonographic imaging of normal and osteoarthritic cartilage. Semin Arthritis Rheum 28:398–403
24. McCune WJ, Dedrick DK, Aisen AM, MacGuire A (1990) Sonographic evaluation of osteoarthritic femoral condylar cartilage. Correlation with operative findings. Clin Orthop Relat Res 254:230–235
25. Chérin E, Saïed A, Pellaumail B, Loeuille D, Laugier P, Gillet P, Netter P, Berger G (2001) Assessment of rat articular cartilage maturation using 50-MHz quantitative ultrasonography. Osteoarthritis Cartilage 9:178–186

Published OnlineFirst October 7, 2011; DOI:10.1158/0008-5472.CAN-11-2389

Cancer Research

Volumetric and Angiogenic Evaluation of Antitumor Effects with Acoustic Liposome and High-Frequency Ultrasound

Tetsuya Kodama[1], Noriko Tomita[1,3], Yoko Yagishita[2], Sachiko Horie[1], Kenichi Funamoto[3], Toshiyuki Hayase[3], Maya Sakamoto[4], and Shiro Mori[4]

Abstract

Acoustic liposomes (AL) have their inherent echogenicity and can add functionality in serving as drug carriers with tissue specificity. Nonuniform vascular structures and vascular branches/bends are evaluated by imaging the intravascular movement locus of ALs with high-frequency ultrasound (HF-US) imaging. However, the evaluation of antitumor effects on angiogenesis by ALs and HF-US imaging has not been reported. Here, we show that the combination of ALs and an HF-US imaging system is capable of noninvasively evaluating antitumor volumetric and angiogenic effects in preclinical mouse models of various cancers. In this study, the antitumor effects of cisplatin on tumor growth and angiogenesis in mice bearing two different types of tumor cells were assessed. By tracking each AL flowing in the vessel and transferring the images to personal computers, microvessel structures were mapped and reconstructed using the color difference based on SD method. The antitumor effects were confirmed with an *in vivo* bioluminescence imaging system and immunohistochemical analysis. Our results show that cisplatin inhibits tumor growth by decreasing intratumoral vessel area but does not affect the angiogenesis ratio in the tumor. The vascular occupancy in the outer region of the tumor was larger than that in the inner region; however, both occupancies were similar to those of the control tumor. We propose that this method of mapping microvessels with ALs and an HF-US system can serve as a new molecular imaging method for the assessment of angiogenesis and can be applied to evaluate the antitumor effects by various therapeutic agents. *Cancer Res; 71(22); 6957–64. ©2011 AACR.*

Introduction

With the development of ultrasound contrast agents (UCA), contrast-enhanced ultrasound can image blood perfusion in organs and measure blood flow rate in the heart and other organs, thereby facilitating the detection of primary and metastatic cancer (1, 2). Acoustic liposomes (AL) are one kind of UCA and can add functionality along with echogenicity, serving as drug carriers with tissue specificity (3–6). When their diameter is reduced to 100 to 200 nm, the enhanced permeability and retention (EPR) effect (7) can be exploited, creating the possibility of using high-frequency ultrasound (HF-US) to evaluate vascular permeability, vascular number, and vascular occupancy by their extravascular US imaging properties. In addition, tumor-targeting chemotherapy can be achieved by collapsing extravascularized ALs with US, that is, sonoporation (4, 6, 8). However, the *in vivo* lifetime of ALs is relatively short compared with that of commercially available UCAs, thus the angiogenic evaluation of antitumor effects with ALs and HF-US imaging has not been reported. In this study, we evaluated tumor volume and vascular area in tumors with and without intratumoral injection of cisplatin (CDDP). Tumors after injected intravenously with ALs were imaged by a HF-US system. Images were evaluated using the color difference based on SD (CDSD) method (9). We found that CDDP induced cytoreductive effects but did not affect the angiogenesis ratio in the tumor. The vascular occupancy in the outer region of the tumor was larger than that in the inner region; however, both occupancies were similar to those of the control tumor (saline injection). The results indicate that CDDP may not inhibit angiogenesis specifically. We propose that this microvessel mapping system can serve as a new molecular imaging method for assessing the effects of therapy on angiogenesis.

Authors' Affiliations: Graduate Schools of [1]Biomedical Engineering and [2]Dentistry, [3]Institute of Fluid Science, Tohoku University; and [4]Tohoku University Hospital, Miyagi, Japan

Corresponding Author: Tetsuya Kodama, Graduate School of Biomedical Engineering, Tohoku University, 2-1 Seiryo, Aoba, Sendai, Miyagi 980-8575, Japan. Phone: 81-22-717-7583; Fax: 81-22-717-7583; E-mail: kodama@bme.tohoku.ac.jp

doi: 10.1158/0008-5472.CAN-11-2389

Materials and Methods

In vivo studies were done in accordance with the ethical guidelines of Tohoku University.

Preparation of acoustic liposomes

The ALs were prepared as described previously (3, 10). The shell composition was 1,2-distearoyl-sn-glycero-phosphatidylcholine (DSPC; NOF Co.) and N- (carbonyl-methoxypolyethyleneglycol-2000)-1,2-distearoyl-sn-glycero-3-phosphoethanolamine (DSPE-PEG2000-Ome; PEG molecular weight, 2,000; NOF Co.; 94:6 (mol/mol). The number of ALs in lipid solution

Published OnlineFirst October 7, 2011; DOI:10.1158/0008-5472.CAN-11-2389

was calculated to be 3.3×10^{12} bubbles/mL (6). The peak diameter of the number distribution was 0.20 ± 0.08 μm and the zeta potential was -2.40 ± 0.51 mV. Approximately 20% of the ALs contained both liquid and gas, whereas approximately 80% contained liquid alone (i.e., nonacoustic; ref. 6).

Tumor cell culture

Murine colon carcinoma (Colon26) cells were obtained from the Cell Resource Center for Biomedical Research, Institute of Development, Aging and Cancer, Tohoku University, on March 28, 2006. Murine mammary carcinoma (EMT6) cells were obtained from American Type Culture Collection on December 4, 2008. Colon26-Luc and EMT6-Luc cells stably expressing of the firefly luciferase gene were prepared by Transfection of Colon26 and EMT6 cells with pEGFP (BD Bioscience) using Lipofection Transfer Reagent (Invitrogen), respectively (11). Colon26 and EMT6 cells were cultured in RPMI 1640 medium and Dulbecco's modified Eagle's medium, respectively, supplemented with 10% FBS and 1% penicillin/streptomycin. Colon26-Luc and EMT6-Luc cells were cultured in each medium added with Geneticin (G418 sulfate; Sigma-Aldrich; 1 mg/mL), respectively. Cells were incubated at 37°C in a mixture of 5% carbon dioxide and 95% air until 80% confluence was achieved. Cells were routinely verified by morphology and growth characteristics using Trypan blue. Cells were tested for *Mycoplasma* contamination on the day of the inoculation, day 0, using MycoAlaert *Mycoplasma* Detection Kit according to the manufacturer's protocol. *Mycoplasma*-negative cells were used for this study.

Tumor model

Colon26, Colon26-Luc, or EMT6-Luc cells were suspended in PBS without Mg_2^+ and Ca_2^+ (PBS). To form solid tumors, 1×10^7 cells/mL of 100 μL was injected intradermally into the right and left flanks of severe combined immunodeficient (SCID) mice (age 6–8 weeks, weight 20–25 g) or BALB/c mice (age 9 weeks, weight 25–27 g), in which the flanks to be injected were depilated with commercial hair removal cream. Colon26 cells were used for the BALB/c mice and Colon26-Luc and EMT6-Luc cells were used for the SCID mice. The day of inoculation was defined as day 0. Tumors were allowed to grow to a diameter of 10 to 15 mm, which was normally attained in 15 to 16 days.

CDDP treatment

For the treated groups, a total of 40 μL CDDP (molecular weight 300, 10 mg/20 mL, Nihon Kayaku Co.) and 60 μL PBS, that is, CDDP of 2 μg/g body weight, was injected in each solid tumor on days 4, 8, and 11 for the EMT6-Luc cells and on days 7, 12, and 15 for the Colon26-Luc cells. In the control group, 100 μL of PBS was injected intratumorally under the same conditions as for the treatment group (12). For the EMT6-Luc cells, tumor-bearing mice in the treatment group numbered $n = 21$, and in the control group, $n = 12$. For Colon26-Luc tumor-bearing mice in the treatment, $n = 9$, and in the control group, $n = 9$.

Tumor growth assessment

Two methods, an *in vivo* bioluminescence imaging system and the HF-US imaging system, were used for tumor growth assessment on day 4 ($n = 12$ for control, $n = 9$ for treatment), day 8 ($n = 9$ for control, $n = 9$ for treatment), day 11 ($n = 6$ for control, $n = 6$ for treatment), and day 15 ($n = 3$ for control, $n = 3$ for treatment) for the EMT6-Luc cells, and on day 4 ($n = 9$ for control, $n = 9$ for treatment), day 7 ($n = 9$ for control, $n = 9$ for treatment), day 12 ($n = 6$ for control, $n = 6$ for treatment) and day 15 ($n = 3$ for control, $n = 3$ for treatment) for the Colon26-Luc cells. With the bioluminescence imaging method, the luminescence intensities were assessed with the *in vivo* imaging system, IVIS Lumina (Caliper Life Science Inc.; refs. 6, 12). With the HF-US imaging method, B-mode images were acquired with the Vevo 770 system (VisualSonics Inc.) under room temperature of 22°C to 26°C. The scanner was equipped with a mechanical single element transducer (RMV-704, central frequency 40 MHz, axial resolution 40 μm, lateral resolution 80 μm, slice thickness resolution 40 μm, focal depth 6 mm, and length of field 1.5 mm). The transducer was fixed with a 3-dimensional (3D) stage control system (mark-204-MS; Sigma Koki). Mice were anesthetized with 2% isoflurane (Abbott Japan Co., Ltd.) and placed on a stage maintained at 38°C (TM150, VisualSonics Inc.). To maintain US transmission, US gel (Parker Laboratories Inc.) was placed on the tumor formed in the flank. In the tumor images, linear measurements were made across each axis to measure the length, width, and depth of the tumor. The center of the tumor was set at the focal length. 2D/3D images of the tumor were constructed by B-mode images. 2D B-mode images at the center of the longitudinal length were acquired at 30 frames/sec for 10 seconds, that is, the obtained cineloops consisted of 300 frames. The consecutive B-mode images acquired with a slice thickness of 100 μm, scanning across the tumor by the computer-controlled 3D motorized stage, were reconstructed into a 3D image, and the volume consisting of multiple polygons was calculated with the Vevo 770 software.

Evaluation of time-dependent changes in grayscale intensity in tumors

Time-dependent changes in the grayscale intensity of mouse solid tumors were investigated. With the HF-US imaging method, B-mode images were acquired at the center of tumors using the HF-US imaging system with a 40 MHz transducer on day 8, as described in the previous section. ALs were used as an US contrast agent and were prepared 1 minute before each injection, as previously described. Colon26 tumor-bearing mice ($n = 4$) were given bolus intravenous injection of ALs (lipid concentration: 1 mg/mL) via the tail vein for a total volume of 100 μL. B-mode images were acquired from approximately 5 seconds before AL injection. The tumor grayscale intensities in each frame were calculated using the HF-US system software.

Reconstruction of intratumoral microvasculatures using ALs

The 2D images of intratumoral microvasculature were reconstructed in only one solid tumor per mouse on day 5 ($n = 9$ for control, $n = 9$ for treatment), day 9 ($n = 3$ for control, $n = 3$ for treatment), day 12 ($n = 6$ for control, $n = 6$ for treatment), and day 15 ($n = 3$ for control, $n = 3$ for

Published OnlineFirst October 7, 2011; DOI:10.1158/0008-5472.CAN-11-2389

treatment) for the EMT6-Luc cells, and on day 8 ($n = 3$ for control, $n = 3$ for treatment), day 13 ($n = 3$ for control, $n = 3$ for treatment), and day 16 ($n = 3$ for control, $n = 3$ for treatment) for the Colon26-Luc cells. The lifetime of the ALs was maintained to about 6 minutes after intravenous injection. The B-mode images of the tumor were obtained with the HF-US imaging system between 20 and 90 seconds (i.e., diagnostic window) after ALs injection. A B-mode image consisting of 300 frames (434MB in AVI format), with a frame interval of 100 μm, was divided into 300 individual frames in BMP format (423 MB) with a video encoding software (TMPGEnc Free Version; Pegasys Inc.). Each image was transferred to a computer system (SGI Altix 3700 B × 2; SGI Japan) at the Advanced Fluid Information Research Center, Institute of Fluid Science, Tohoku University and analyzed to construct maps of 2D microvasculature by using the CDSD method (9). In the CDSD method, the lumen of a blood vessel is recognized by detecting an instantaneous increase of brightness due to ALs passing through the vessel, with a threshold value defined by the time-average and the SD of the brightness. Compared with the conventional visualization method (13), this approach is capable of visualizing vascular regions by suppressing the effects of noise and tissue movement in US B-mode measurements. The differences in image brightness between pre- and postinjection of the ALs were displayed using ImageJ software (14). The image was binarized to enhance the vascular structure. One scan per solid tumor was done.

Immunohistochemical analysis

The solid tumors that were used for the vessel map construction as described above were then excised. The blocks used for immunohistochemical staining were fixed in 4% neutral buffered formalin (Wako Pure Chemical Industries) for 2 to 3 days at 4°C, embedded with Paraplast (Thermo Fisher Scientific K.K.), sectioned into 3 to 3.5 μm sections, and deparaffinized with the Tissue clear (Sakura Finetck Japan Co., Ltd.). CD31-positive endothelial cells were stained with anti-mouse CD31 rabbit polyclonal antibody as a primary antibody (dilution with 1% bovine serum albumin in PBS solution, 1:50; Abcam plc.). A peroxidase conjugated anti-rabbit antibody (Nichirei) was used as a secondary antibody. The sections were stained with 0.04% hydrogen peroxide and 0.2% 3′,3′-diaminobenzidine (Ventana Japan K.K). The hotspot method was used for calculating the vascular ratio (15, 16). First the tumor boundary was extracted under a microscope (BX51; Olympus) with a digital camera (DP72; Olympus) at a low magnification (×40 or ×100), as shown in Fig. 4A. Next, the boundary was reduced by half, and the inner and other regions were defined as Ac and Ao, respectively. Each region was divided into 4 subregions. In Ac region, the mean vascular density was calculated by dividing the vascular total area, consisting of vasculatures with a minor axis of 7 to 50 μm (×200), by the CD31-positive hotspot area (430 μm × 330 μm). Similarly, the mean vascular density in Ao was calculated. The vascular density measurement was done by 2 persons to reduce measurement error.

Statistical analysis

All measurements are expressed as mean ± SEM. Any overall difference between the groups was determined by 1-way ANOVA. Simple comparisons of the independence of data of 2 groups were done using Student t test or Aspin–Welch t test. Normally distributed equal variables were compared by the Student t test, and normally distributed unequal variables were compared by Aspin-Welch t test. Nonnormally distributed variables were compared by the Mann–Whitney U test. The differences were considered significant at $P < 0.05$.

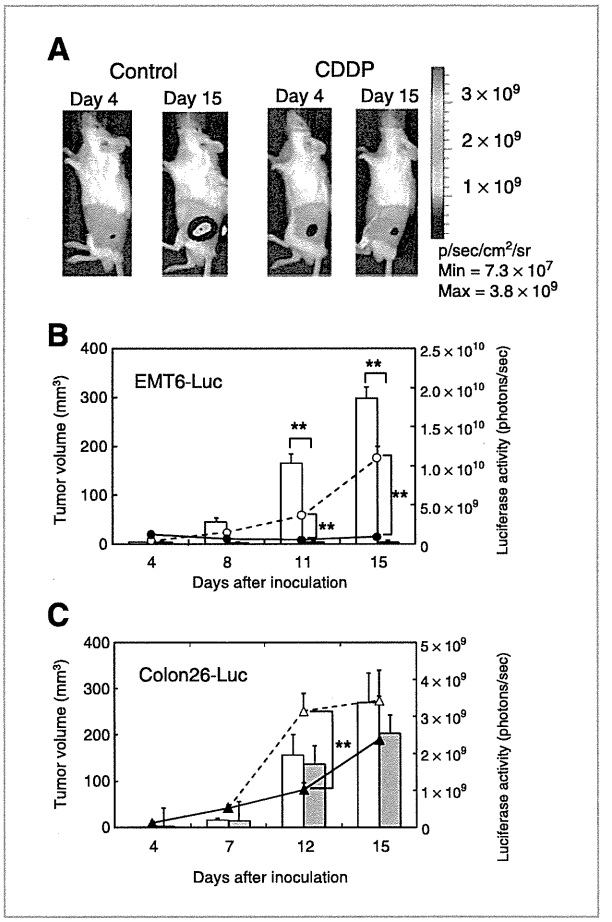

Figure 1. Assessment of antitumor effect by CDDP using the *in vivo* bioluminescence imaging system and the HF-US imaging system. A, representative photographs of the EMT6-Luc tumor on days 4 and 15 with and without CDDP treatments. B, EMT6-Luc tumor. Open and closed circles represent the mean tumor volumes of the control and CDDP treatment groups, respectively. White and gray bars indicate the luciferase activity of the control and CDDP treatment groups, respectively. C, Colon26-Luc tumor. Open and closed triangles represent the mean tumor volumes of the control and CDDP treatment groups, respectively. White and gray bars indicate the luciferase activity of the control and CDDP treatment groups in both tumors, respectively. In the EMT6-Luc tumor, significant differences in tumor volume were detected on days 11 ($P < 0.01$; Student t test) and 15 ($P < 0.01$; Aspin–Welch t test). Significant differences were detected in the luciferase activity on days 11 ($P < 0.01$; Aspin–Welch t test) and 15 ($P < 0.01$; Aspin–Welch t test). In the Colon26-Luc tumor, a significant difference in the luciferase activity was detected on day 12 ($P < 0.01$; Aspin–Welch t test). **, $P < 0.01$.

Published OnlineFirst October 7, 2011; DOI:10.1158/0008-5472.CAN-11-2389

Results

Evaluation of CDDP-induced cytoreductive effect with the HF-US imaging system and the bioluminescence imaging system

The CDDP-induced cytoreductive effects were assessed by using the HF-US imaging system and bioluminescence imaging system up to 15 days postimplantation of tumor cells (Fig. 1). We measured the minimum volume V_{min} = 3.3 mm^3 (using volume = $\pi D_e^3/6$, in which D_e = equivalent diameter of a sphere with the same volume, and D_e = 1.8 mm) to the maximum volume V_{max} = 153 mm^3 (D_e = 6.6mm) for the EMT6-Luc tumor (Fig. 1B), whereas for the Colon26-Luc tumor, V_{min} ranged from 4.8 mm^3 (D_e = 2.1mm) to V_{max} = 320 mm^3 (D_e = 8.5 mm; Fig. 1C). As shown in Fig. 1A and B, the EMT6-Luc tumor volumes (Fig. 1B, open circle) and the luciferase activities (white bar) increased in the control group over time; however, they were inhibited in the CDDP treatment group (solid circle, volume; gray bar, luciferase activity). On days 11 and 15, the mean volumes of the treatment groups were significantly lower than those of the control groups ($P < 0.01$, Aspin–Welch t test). Also, on days 8, 11, and 15, the mean luciferase activities of the treatment groups were significantly lower than those of the control groups ($P < 0.01$, Aspin–Welch t test). For the Colon26-Luc tumors (Fig. 1C), the tumor growth was suppressed by the treatments. However, the cytoreductive effects were lower than in the EMT6-Luc tumor; that is, for the EMT6-Luc tumor, the mean volume and the luciferase activity of the treatment group on day 15 decreased by approximately 1/10th compared with that of the control group. However, in the Colon26-Luc tumors, by day 15, the mean volume and the luciferase activity of the CDDP treatment group decreased by only 60% and 70% of those in the control group, respectively.

Time–intensity relation of ALs in tumors and constructed vascular images by ALs, HF-US image system, and the CDSD method

To determine the optimal diagnostic window allowed to capture vascular imaging in the presence of ALs, we investigated the time–intensity relation of B-mode images of tumors injected with ALs. Figure 2A shows a representative time–intensity relation in tumors of Colon26 on day 8 in the absence of CDDP. Immediately after the AL tail vein injection, the mean grayscale value increased dramatically and then decreased gradually to the background level within 6 minutes. The half-life of ALs *in vivo* was 84 ± 12 seconds (n = 4). The vasculatures were clearly constructed between 20 and 90 seconds after tail vein injection of ALs. In the following experiments, the optimal diagnostic window allowed to capture all HF-US images was set between these times. Figure 2B shows representative 2D images of the Colon26-Luc tumor on day 8 without CDDP treatment (control). The intratumoral vasculatures were constructed by ALs, the HF-US image system and the CDSD method. Figure 2Ba and c show a B-mode image of tumor before AL injection and its corresponding extracted 2D vascular structures, respectively. Figure 2Bb and d indicate that of tumor after AL injection and its extracted 2D vascular structures, respectively. Although Fig. 2Bb shares a similar image with Fig. 2Ba at first glance, the CDSD method is capable of extracting 2D vascular structures from animated images of Fig. 2Bb, as shown in Fig. 2Bd, by detecting an instantaneous increase of brightness due to ALs passing through the vessel.

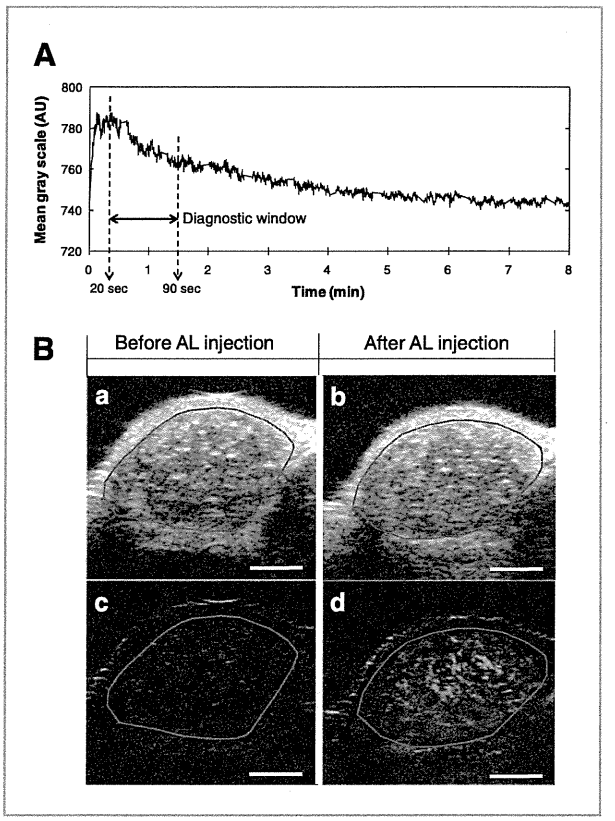

Figure 2. Construction of intratumoral vessels with the combination of ALs, the HF-US imaging system, and the CDSD method. A, representative time-dependent changes in grayscale intensity in tumors of Colon26 without CDDP treatment. After the injection of ALs, significantly higher grayscale intensity was observed and maintained for approximately 6 minutes. An optimal diagnostic window for detection of ALs was established between 20 and 90 sec postinjection. B, representative 2D images of the Colon26-Luc tumor on day 8 without CDDP treatment (control). (a) and (b) are B-mode images of tumor before and after AL injection, respectively. (c) and (d) are the extracted 2D vascular structures in tumor before and after AL injection, respectively. The image was constructed from the B-mode image using the CDSD method. The margins of the tumor areas are delineated by red lines and scale bars indicate 1 mm.

Angiogenic evaluation by ALs, the HF-US image system, and the CDSD method

We quantified the CDDP-induced longitudinal angiogenesis suppression using the combination of ALs, the HF-US imaging system, and the CDSD method. In the EMT6-Luc tumor (Fig. 3A), the tumor area (Cont. TA) and vessel area (Cont. VA) increased in the control group over 15 days, but the tumor area (CDDP TA) and vessel area (CDDP VA) decreased in the CDDP treatment group. Similarly, in the Colon26-Luc tumor (Fig. 3B), the growth of the tumor area (CDDP TA) and vessel